Voltage Sensor Conformations Induced by LQTS-associated Mutations in hERG Potassium Channels

Aaron N. Chan[2], Lucas J. Handlin[1], Erin N. Lessie[1], Emad Tajkhorshid[2], and Gucan Dai[1,*]

Author Affiliations:

[1]Department of Biochemistry and Molecular Biology, Saint Louis University School of Medicine

[2]Theoretical and Computational Biophysics Group, NIH Center for Macromolecular Modeling and Visualization, Beckman Institute for Advanced Science and Technology, Department of Biochemistry, and Center for Biophysics and Quantitative Biology, University of Illinois at Urbana-Champaign

*Correspondence: gucan.dai@health.slu.edu

ABSTRACT

Voltage sensors are essential for electromechanical coupling in hERG K^+ channels, critical to cardiac rhythm. These sensors detect changes in membrane voltage and move in response to the transmembrane electric field. Mutations in voltage-sensing arginines of hERG, associated with Long QT syndrome, alter channel gating, though mechanisms in these mutants remain unclear. Using fluorescence lifetime imaging microscopy (FLIM), transition metal FRET (tmFRET), dual stop-codon mediated noncanonical amino acid incorporation, and molecular dynamics (MD) simulations, we identified distinct intermediate voltage-sensor conformations caused by these mutations. Phasor plot analysis of the FLIM-tmFRET donor revealed multiple FRET states in mutant hERG channels, in contrast to the single high-FRET state observed in unmutated controls. These intermediate FRET states correspond to specific mutation sites and align with distinct intermediate voltage-sensor conformations identified in MD simulations. This study provides novel insights into cardiac channelopathies, highlighting structural underpinnings underlying voltage sensing in cardiac arrhythmias.

INTRODUCTION

Voltage sensing of ion channels is crucial for regulating cardiac and neuronal excitability[1]. Voltage sensors detect changes in membrane voltage, thereby initiating conformational changes that govern the opening and closing of voltage-gated ion channels (VGICs)[1,2]. This pivotal role allows VGICs to precisely control the flux of ions across cell membranes, thereby orchestrating essential physiological processes such as action potentials in neurons, muscle contraction, cardiac pacemaking, and secretion of neurotransmitters. Notably, dysfunction of ion channels is implicated in various disease states, including the prolonged QT-interval syndrome (long QT syndrome, LQTS), a cardiac disorder characterized by prolonged ventricular repolarization, which can cause life-threatening arrhythmias. Mutations in the human ether-à-go-go-related gene (hERG), which encodes the cardiac potassium channel Kv11.1, represent a prevalent cause of congenital LQTS[3,4]. The hERG channel, belonging to the voltage-gated ion channel (VGIC) superfamily, features a functional voltage sensor, where mutations linked to LQTS have been identified[5].

Voltage sensors of VGICs are characterized by repeats of positively charged arginines within the 4th transmembrane helix (S4), which directly sense the transmembrane electric field[2]. The function of the S4 relies on its significant "up and down" movements[2,6-12]. The precise conformational changes associated with these movements are critical for channel gating in response to electrical fluctuations across the membrane, a process referred to as electromechanical coupling. The up conformations of the S4 were first captured in the absence of voltage difference[2,13,14]. In comparison, high-resolution structures capturing the down conformation, which corresponds to the S4 voltage sensor at resting hyperpolarized membrane potentials, have been notably difficult to resolve. This conformation was first observed in an *Arabidopsis* two-pore channel (TPC)[6]. Similar down conformations have been identified in other VGICs such as voltage-gated sodium channels and pacemaker hyperpolarization-activated cyclic nucleotide-gated (HCN) channels[7-10,15]. Furthermore, cryo-electron microscopy (cryo-EM) studies have provided atomic-level insights into voltage sensors under hyperpolarizing conditions. This was achieved by reconstituting the channels into liposome membranes and manipulating ionic gradients to apply hyperpolarizing voltages, ideally while the channel pores remained closed[11,12]. Particularly, cryo-EM structures of ether-à-go-go (Eag) channels, a close relative of hERG, have revealed multiple states including up, down, and intermediate conformations[11]. However, studying the conformational dynamics and heterogeneity of these S4 voltage-sensor states under more native membrane environments remains a significant challenge. A more comprehensive understanding of the structural dynamics and potential multi-step movements of the voltage sensor is crucial for elucidating the electromechanical coupling governing VGIC function.

While fluorescence imaging stands as a valuable tool for understanding the structural mechanisms of voltage sensors, significant technical hurdles arise in controlling membrane voltage for such imaging experiments. Single-molecule fluorescence techniques hold promise, with their capacity to discern distinct protein conformational states, yet their application in probing the voltage-dependent structural arrangements of VGICs remains limited in a native membrane[16,17]. Understanding the structure-function relationship of VGICs often necessitates live-cell imaging, particularly as voltage sensor dynamics depend on membrane lipids in their native environments. Traditional fluorescence intensity-based ensemble imaging, while highly sensitive, tends to homogenize signals when assessing numerous molecules within living cells. Conversely, emerging fluorescence lifetime-based imaging methodologies, such as fluorescence lifetime imaging microscopy (FLIM), have potential to effectively dissect diverse populations of measured molecules exhibiting different conformations[18-21].

In this study, we employed a combination of techniques including nonsense suppression-mediated incorporation of noncanonical amino acids for site-specific fluorescence labeling, FLIM-based transition metal Förster resonance energy transfer (FLIM-tmFRET), and MD simulations to examine the impact of a LQTS-associated mutation on conformational rearrangements of hERG voltage sensors in transfected cell lines. We applied a dual stop-codon suppression strategy relying on a small fluorescent noncanonical amino acid to discern and dissect the conformational heterogeneity of voltage sensors by analyzing the frequency-domain phasor plot function of FLIM-tmFRET. This methodology has significant potential for broad applications, offering an effective approach to quantitatively assess the movement, states, dynamics, and energetics of voltage sensors in ion channels.

RESULTS

Functional impact of S4 helix LQTS mutations on hERG channel gating

The hERG (K_v11.1 or KCNH2) channels expressed in tsA-201 cells exhibit a depolarization-dependent activation profile like other voltage-gated potassium channels[1]. Within the S4 helix of hERG, six positively charged arginines or lysines are present, with the arginines likely serving as the primary voltage-sensing residues (Supplementary Fig. 1a). Notably, mutations of R531 and R534 have been associated with LQTS[5,22].

We generated homology models (SWISS-MODEL) of hERG based on previous findings identifying three distinct conformations of rat Eag channel voltage sensors using cryo-EM techniques[11,23]. In the down state model at hyperpolarized voltages (Supplementary Fig. 1b), only the side chain of K525 of hERG is positioned above the "phenylalanine cap", F463, at the hydrophobic constriction site. Upon membrane depolarization, the side chains of K525, R528, and R531 are predicted to relocate above the phenylalanine cap. In comparison, in the model of the hypothetical intermediate state, the side chains of K525 and R528, but not that of the R531, are positioned above the phenylalanine cap. We postulate that this intermediate state may represent an important point along the trajectory of the voltage sensor movement within hERG channels.

In the presence of 10 mM tetraethylammonium (TEA) to fully inhibit endogenous potassium currents in tsA cells[24] (Supplementary Fig. 1c) - different from the wild-type (WT+; with S620T) hERG channels[25] - LQTS-associated hERG-R531Q channels demonstrated a noticeable initial phase of approximately 100 ms, preceding the delayed second phase (Fig. 1a). This delay in hERG currents demonstrates the functional impact of the R531Q mutation in LQTS development. The S620T mutation near the selectivity filter eliminates C-type inactivation in hERG channels, allowing the activation profile to be analyzed independently from the inactivation[25-27]. The activation profile was plotted using the instantaneous "tail current" amplitudes at -100 mV during repolarization at the end of the voltage protocol (Fig. 1a and b). Examining the tail current amplitude in relation to applied voltages revealed a substantial right shift in the conductance-voltage (G-V) relationship compared to that of wild-type channels (Fig. 1b); the voltage of the half maximal activation for the R531Q mutant channel was +81 ± 3.7 mV (n = 4) compared to +35 ± 2.8 mV (n = 8) for the WT channel. This approximately 45 mV shift in the G-V and the biphasic channel activation are consistent with prior research and indicative of potential intermediate functional states for the R531Q mutant[22,28]. Furthermore, this initial lag was shorter in hERG-R528Q channels, followed by a double-exponential main current phase for the activation; the deactivation was much slower (Supplementary Fig. 1d). The R528Q mutation did not significantly shift the G-V relationship ($V_{1/2}$ = + 24 ± 7.7 mV, n = 4) compared to the WT and has not been linked to LQTS. Additionally, LQTS-linked mutations R534L or R534Q produced hERG channels that have diminished multi-phasic activation kinetics, instead displaying noticeable voltage-induced channel inactivation (Supplementary Fig. 1e). Assessing the functional impact of these three charge-neutralization mutations on channel activation, the R531Q produces the most significant effect. This result is consistent with the finding that R531 is the primary residue that contributes to the smaller total gating charge of 1.5 elementary electronic charges per subunit, compared to classic voltage-gated potassium channels[28-30].

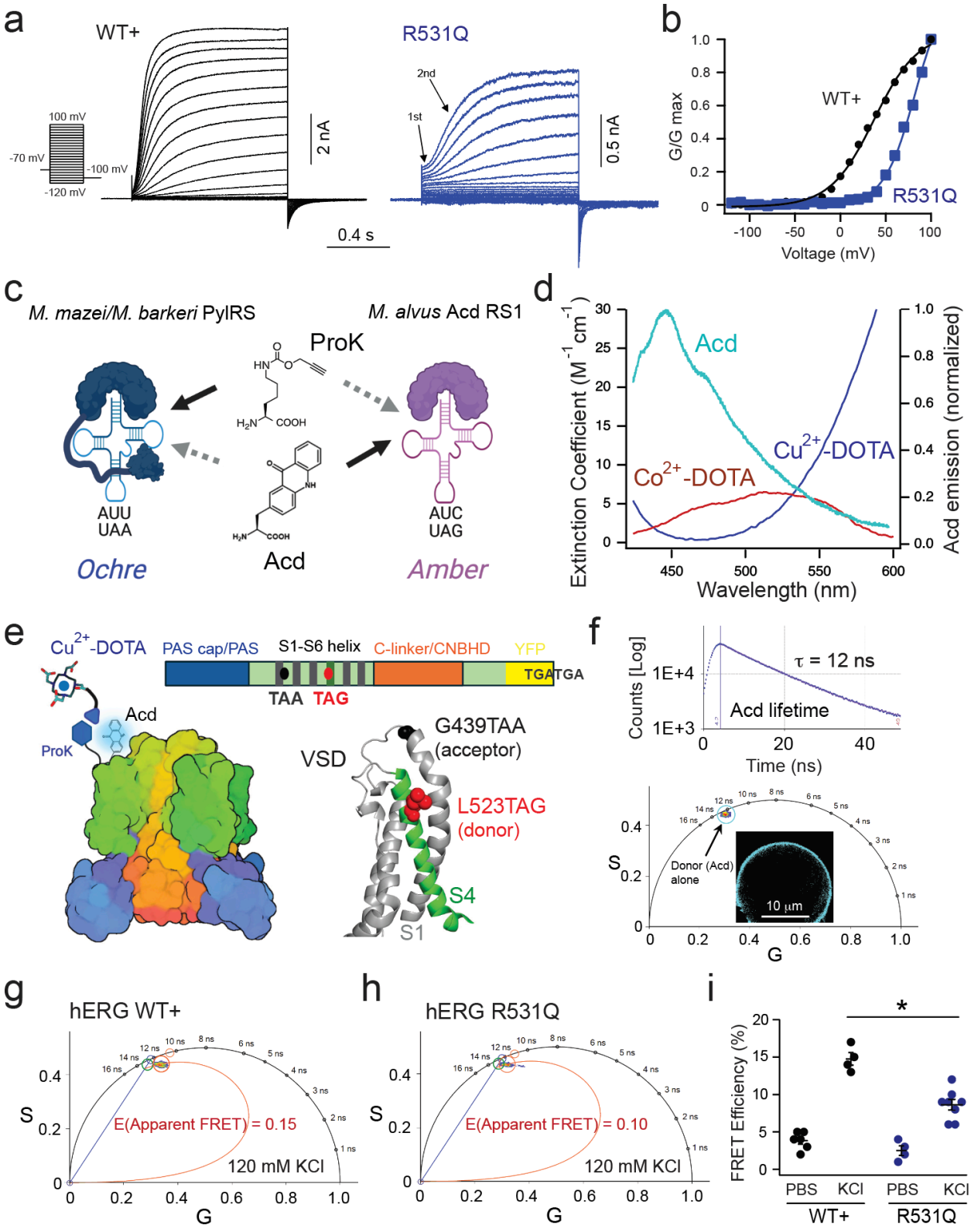

Fig. 1. Effects of the R531Q mutation on hERG gating and the design of phasor FLIM-tmFRET strategies for measuring voltage sensor movement in WT+ and R531Q hERG channels.

a. Representative current traces for activation of WT+ (S620T) hERG1 channels, elicited by steps of depolarizing voltage pulses from -120 mV to +100 mV. Tail currents were recorded at -100 mV. Also shown are representative current traces for activation of hERG1-R531Q channels, produced using the same voltage protocol. **b**. Comparison of conductance-voltage (G-V) relationships for activation of hERG WT and hERG-R531Q channels. **c**. Diagram illustrating the dual stop-codon (amber and ochre) suppression for incorporating Acd and ProK in a mutually orthogonal manner. **d**. Absorption and emission spectra showing the spectral overlap between the Acd emission incorporated to hERG channels (L523 site) and the molar absorption of Co^{2+} or Cu^{2+} coordinated with azido-DOTA. **e**. Design of a tmFRET pair with the FRET donor positioning in the L523TAG site of the S4 helix and the FRET acceptor in the C-terminal end of the S1 helix (near the S1-S2 linker). YFP not shown in the structural cartoon. **f**. Mono-exponential lifetime decay of Acd when incorporated into the L523 site. The lifetime species of membrane localized Acd can also be displayed in the phasor plot, with $\tau(\varphi)$ = 11.7 ns and $\tau(m)$ = 12.6 ns. The slight deviation of the Acd lifetime species from the universal semicircle is due to background contribution, typically 2% - 5%. **g**. FRET trajectory calculation enabled by the phasor plotting for hERG WT+ channels (hERG-WT with S620T and the L523TAG and G439TAA mutations), labeled with Cu^{2+} acceptor via CuAAC click chemistry in the presence of 120 mM extracellular KCl. **h**. Similar FRET trajectory calculation for hERG-R531Q channels as a comparison. **i**. Summary data showing the apparent FRET efficiency of hERG WT+ and hERG R531Q channels, either in regular PBS solution or with 120 mM KCl, using the FRET trajectory method as in panels g and h. Data shown are mean ± s.e.m., n = 4 – 8, *p = 4e-5 at KCl conditions using one-way ANOVA (no adjustment).

Measuring the movement of voltage sensors in hERG channels using FLIM-tmFRET

To advance our structural investigation of the impact of LQTS mutations on hERG gating, we implemented a dual stop-codon suppression strategy to incorporate noncanonical amino acids for site-specific fluorescence labeling and FRET measurements of voltage-sensor movements[31]. We modified a human hERG1 construct by introducing amber (TAG) and ochre (TAA) stop codons at selected positions within the voltage-sensing domain (VSD) of hERG channels (Fig. 1). The amber stop-codon suppression approach facilitated the incorporation of a fluorescent noncanonical amino acid L-acridonyl-alanine (Acd) into the S4 helix[32,33]. This was achieved using a recently developed Acd tRNA/tRNA synthetase system adapted from the pyrrolysyl-tRNA synthetase of the archaeon *Methanomethylophilus alvus (M. alvus)* [33] (Fig. 1c). Importantly, this orthogonal strategy operates independently of the ochre stop-codon suppression system, which is derived from the pyrrolysyl-tRNA synthetase of the *Methanosarcina* archaea *M. mazei*/*M. barkeri*[34]. Specifically, we used a tRNA (M15-PylT)/PylRS pair derived from *M. mazei*/*M. barkeri* to introduce N-propargyl-L-lysine (ProK) into another relatively immobile site within the VSD. ProK features an alkyne group capable of undergoing specific chemical reactions with azide-containing compounds via copper(I)-catalyzed azide-alkyne cycloaddition (CuAAC) click chemistry. Previously, we have applied a similar approach to perform FLIM-tmFRET experiments for HCN channels[31,34], with the integration of Acd marking a notable enhancement over our prior dual stop-codon suppression methodology. Furthermore, this protein labeling design circumvents the necessity for cysteine-based labeling, mitigating potential concerns of mutating endogenous cysteine residues (~160) within hERG channels.

We designed a tmFRET pair comprising Acd as the FRET donor and Cu^{2+} chelated by 1,4,7,10-tetraazacyclododecane-1,4,7,10-tetraacetic acid (DOTA) as the FRET acceptor. The emission spectrum of Acd overlaps with the absorption spectrum of Cu^{2+} or Co^{2+} coordinated by an azido mono-amide-DOTA (Fig. 1d). The weak molar absorption of transition metals results in a shorter Förster distance (R_0 = ~ 10 – 20 Å, depending on the exact design) for tmFRET compared to conventional FRET pairs[20,21,35-37]. This reduced working distance of tmFRET is well-suited for investigating voltage-sensor movement in ion channels[9,10,31,38]. For probing the S4 movement of hERG channels, we positioned the Acd site at the L523 position near the N-terminal side of the S4 helix and the ProK/Cu^{2+}-DOTA site at the G439 position at the C-terminal end of the S1 helix (Fig. 1e). This design is predicated on the premise that the FRET donor and acceptor should be distant enough when the S4 is in the down state, resulting in minimal FRET, and exhibit increased FRET when they approach due to membrane depolarization. Because of the short R_0 of this tmFRET pair, FRET occurs primarily within the same subunit; inter-subunit FRET is negligible[9,10,31]. Additionally, all the hERG constructs had a YFP to the C-terminal end of the channel to indicate the expression of full-length proteins at the cell membrane. Our observations revealed a correlation between YFP fluorescence and Acd fluorescence, confirming the expression of hERG channels (Supplementary Fig. 2). Functionally, for hERG channels with Acd and ProK incorporated (hERG-G439TAA/L523TAG-YFP construct), similar depolarization-dependent activation was observed, with R531Q significantly rightward shifted the G-V relationship compared to the control (Supplementary Fig. 2).

Phasor FLIM was used to quantify the tmFRET by measuring the lifetime of Acd in tsA cells. One advantage of Acd is its exceptionally long and mono-exponential lifetime (~16 ns free in solution and ~12 ns when incorporated in cells)[20]. Both time-domain and frequency-domain types of FLIM were performed, which yielded similar lifetime values for the membrane-localized fluorescence coming from the Acd incorporated at the L523 position of the S4 helix (Fig. 1f). In the phasor plot of frequency domain FLIM, the lifetime data for each pixel in the confocal image were translated on a Cartesian coordinate, delineated by a universal semicircle (Fig. 1f)[18,39,40]. Fourier transformation was involved; thus, the x-axis represents the real (G) component while the y-axis represents the imaginary (S) component of the lifetime decay information. Mono-exponential lifetimes precisely aligned with the semicircle, whereas multiexponential lifetimes localize within it. Shorter lifetimes demonstrate a clockwise shift along the semicircle. Considering a small amount of background contribution, the measured Acd phasor in cells is nearly on the semicircle, meaning its lifetime is close to mono-exponential, which facilitates our subsequent FRET analysis.

We used the FRET trajectory function facilitated by the phasor approach of FLIM to assess the change in tmFRET, comparing tsA cells expressing hERG channels imaged in either regular phosphate-buffered saline (PBS) or a depolarizing solution containing 120 mM KCl (Fig. 2 g-i). This function relies on the concept that the degree of shortened donor lifetime reports FRET efficiency, thereby representing the distance between the FRET donor and acceptor. The FRET trajectory starts from zero FRET efficiency, aligning with the donor-alone reference, and follows a path through the measured phasor species, ending at the theoretical 100% FRET efficiency at the origin (0, 0) coordinate, where most of the background noise is situated (Supplementary Fig. 2b). For hERG-G439TAA/L523TAG-YFP channels (also referred to as WT+ denoting no additional mutations), FRET efficiency was minimal in PBS as expected but increased upon exposure to 120 mM KCl. In addition, treatment of 120 mM KCl did not affect the lifetime of the Acd donor alone. Conversely, in comparison to the WT+, the presence of R531Q in the hERG construct produced a similarly low FRET efficiency in PBS, but the increase in FRET after the high KCl was attenuated (Fig. 1i). This outcome corresponds to the rightward shift observed in the G-V curve of the hERG-R531Q channels, indicating a compromise in the extent or likelihood of voltage sensor movement.

However, while the FRET trajectory method used in ensemble imaging experiments offers valuable insights, it also comes with limitations. Although it provides a quantified FRET efficiency, it only represents an averaged distance between donors and acceptors, lacking the capacity to reveal more detailed structural information and the conformational heterogeneity of the S4 helix. This limitation hinders its ability to effectively test hypotheses regarding the presence of intermediate states of hERG channel voltage sensors and evaluating the potential impact of the R531Q mutation on distinct conformational states of the voltage sensor. Moreover, FRET trajectory is often inadequate for fitting the distribution of measured lifetime species in the phasor plot. To better interpret data, we used an alternative approach, leveraging phasor plot analysis of FLIM[18,40].

Probing the conformational heterogeneity of hERG voltage sensors using the phasor approach of FLIM

This alternative analysis leverages the linear unmixing property of the FLIM phasor plot[18,19,39,40]. We consider a voltage sensor with two states: up and down states. The down-state model of the S4 corresponds to the low FRET state, while the up-state model corresponds to the high FRET state (Fig. 2a). In our tmFRET design, the low FRET state, occurring when the distance between the donor and acceptors exceeds ~25 Å, yields nearly negligible FRET, which essentially makes the donor lifetime

nearly unchanged compared to the donor alone situation. Consequently, the measured FRET comprises a mixture of low and high FRET states, and the location of the measured lifetime is primarily determined by the probability of the voltage sensor being in the high FRET state.

To demonstrate linear unmixing in the phasor plot, we used cells expressing the hERG-L523TAG/G439TAA construct, dually labeled with Acd and Cu^{2+}-DOTA (Fig. 2b). Under depolarizing conditions achieved with 120 mM external KCl, the measured FRET can be resolved into two contributors: the donor alone and the position of lifetime if 100% of the voltage sensors are in the high FRET state (Fig. 2b). The linear fitting depends on the pattern of lifetime distribution, resembling a linear trend traversing the major axis of the 'oval' shape formed by lifetime species originating from membrane-localized pixels in the phasor plot (Fig. 2b). This phenomenon likely emerges from the conformational heterogeneity among numerous channel molecules, each adopting various S4 conformational states. In this context, a more pronounced major axis (a greater length-to-width ratio) of the oval-shaped lifetime distribution may suggest a greater diversity in the population of FRET donor-acceptor distances. The measured high FRET value of 0.53, corresponding to a converted distance of approximately 13 Å, reflects the FRET efficiency of the high FRET state, and an estimation of the donor-acceptor distance in the up-state model. Based on the law of phasor additions[39], the fractional contribution of two or more phasor components is inversely proportional to the distance between the measured lifetime position and each component in the phasor plot. Therefore, the percentage of S4 in the high FRET state can be estimated by analyzing the ratio of distances between the measured lifetime position and each phasor component along the linear fit. As expected, membrane depolarization elevated the proportion of the high FRET state; about 35% of voltage sensors transition to the up state, aligning with the relatively low open probability of wild-type hERG channels at approximately +10 mV, a potential achievable with 120 mM KCl, as previously demonstrated using voltage-sensitive dyes[31] (Fig. 2b).

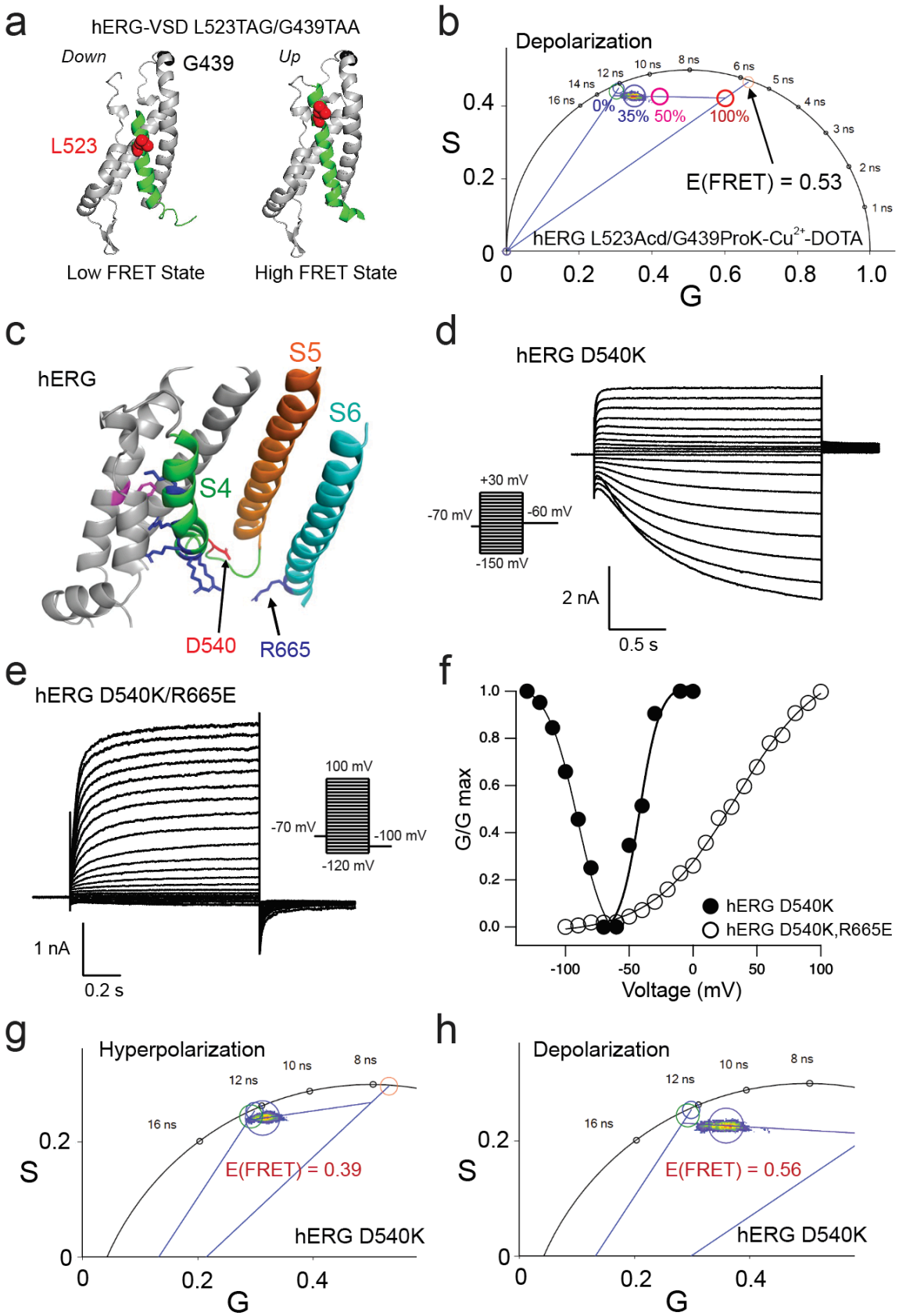
a
hERG-VSD L523TAG/G439TAA
Down
G439
Up
L523
Low FRET State
High FRET State
b
Depolarization
16 ns
14 ns
12 ns
10 ns
8 ns
6 ns
5 ns
4 ns
3 ns
2 ns
1 ns
0%
35%
50%
100%
E(FRET) = 0.53
hERG L523Acd/G439ProK-Cu2+-DOTA
S
G
c
hERG
S5
S6
S4
D540
R665
d
hERG D540K
+30 mV
-70 mV
-60 mV
-150 mV
2 nA
0.5 s
e
hERG D540K/R665E
100 mV
-70 mV
-100 mV
-120 mV
1 nA
0.2 s
f
G/G max
Voltage (mV)
hERG D540K
hERG D540K,R665E
g
Hyperpolarization
E(FRET) = 0.39
hERG D540K
h
Depolarization
E(FRET) = 0.56
hERG D540K

Fig. 2. Applying linear unmixing of phasor analysis to the FLIM-tmFRET for studying hERG channels. **a**. Structural cartoons illustrating the low FRET state and high FRET state in the context of L523TAG/G439TAA FRET pair, corresponding to the homology models of hERG-VSD in the down and up states. Distances between the β carbon of L523 and the α carbon of G439, D(Cβ-Cα), are 31 Å and 22 Å in the down and up states, respectively. The low FRET state yields negligible FRET. **b**. Representative linear unmixing approach to estimate the FRET efficiency corresponding to the high FRET state. The fitting is based on the pattern of lifetime distribution on the phasor plot. The red cursor points to a hypothetical scenario that 100% of voltage sensors are in the up position, and thus the high FRET state. With depolarization via 120 mM KCl, the percentage of voltage sensors in the high FRET state is 35%. The background contribution is 4% for the donor alone (0% FRET) lifetime and 6% in the presence of the acceptor Cu^{2+}-DOTA. **c**. Structural cartoon (upward view) showing the positions of D540 and R665 within the hERG channel. **d-e**. Representative current traces for activation of hERG-D540K and hERG-D540K/R665E charge-swapped channels. **f**. Comparison of G-V relationships for activation of hERG-D540K and hERG-D540K/R665E channels. **g-h**. Combined fluorescence signals from four cells for linear unmixing fitting of hERG-D540K channels in either hyperpolarizing or depolarizing voltage conditions. In the hyperpolarizing condition achieved with extracellular 107 mM NMDG[41], the same tmFRET strategy was employed for analysis. Different FRET efficiencies exhibited when comparing the results from the hyperpolarizing and depolarizing conditions.

We also tested a tmFRET pair using the hERG L523TAG/A430TAA construct (Supplementary Fig. 3). In this case, even in the down state of S4, the proximity of the donor and acceptor resulted in noticeable FRET signals. As a result, the Acd lifetime distribution displayed a distinct arc shape, contrasting with the oval-shaped pattern observed in the hERG L523TAG/G439TAA construct. The primary lifetime distribution (towards shorter lifetime), after a linear fitting, yielded a notably higher FRET efficiency of approximately 0.65 (a converted distance of 10 Å) compared with that of the L523/G439 pair, indicative of a closer donor-acceptor proximity in the L523/A430 pair (Supplementary Fig. 3). In addition, the minor component of the lifetime distribution exhibited a lower FRET efficiency of 0.37 (as indicated by dashed line fitting in Supplementary Fig. 3 b-d, corresponding to a converted distance of 16 Å), presumably corresponding to the FRET in the down state of S4. Upon membrane depolarization, there was a gradual increase in the probability of high FRET, suggesting the upward movement of S4. The presence of this minor component complicated the accurate fitting of the lifetime distribution, especially in the presence of an additional intermediate FRET efficiency, unless a second harmonic of the light modulation frequency was included[42,43]. In addition, since the A430TAA site is more buried in the membrane, the labeling of Cu^{2+}-DOTA might not be complete. Nevertheless, these results emphasize the ability of our FLIM-tmFRET strategy to reliably report S4 movement, with FLIM-tmFRET measurements showing dependence on both donor/acceptor proximity and voltage changes. Since linear unmixing analysis is more effective for a two-state model, particularly when one state shows negligible FRET as seen in the L523/G439 FRET pair, we decided to use the hERG L523/G439 pair for subsequent studies.

We initially conducted proof-of-principle experiments employing phasor analysis to validate the efficacy of this approach. We focused on a single mutation, D540K, which induces a "U-shaped" G-V relationship[44]. Notably, hERG-D540K channels exhibit pronounced hyperpolarization-activated currents

reminiscent of pacemaker HCN channels, alongside depolarization-activated currents (Fig. 2 c-f). This unique G-V profile suggests the presence of multiple conformations of the S4 voltage sensor. In our structural model, the D540K mutation disrupts a critical salt bridge between D540 at the C-terminal end of the S4 and R665 in the C-terminal end of the S6 helix (Fig. 2c). This disruption leads to the decoupling of the S4 and S6, resembling the structural arrangement observed in HCN channels, where the S4 presumably relies on coupling with the S5 helix rather than with the S6 helix for hyperpolarization-dependent activation[9,10,45]. To restore the wild-type behavior of the channel, we engineered a charge-swapping mutant, hERG-D540K/R665E (Fig. 2 e-f), to recreate the salt bridge and thereby reestablish the S4-S6 coupling[44]. This intervention successfully rescued the native function of hERG channels.

Introducing the D540K mutation to engineered hERG channels with the L523/G439 tmFRET pair revealed distinct FRET efficiencies under hyperpolarized versus depolarized membrane conditions (Fig. 2 g-h and Fig 3). In the absence of D540K (hERG-WT+) or with the combined D540K/R665E mutations, only a single high-FRET state was detected, regardless of voltage (Fig. 3 a and c). Increasing the membrane voltage led to a higher proportion of the high-FRET state, with little impact on the amplitude of the FRET efficiency (Fig. 3 a, c, f). These results suggest that for hERG WT+ channels, there exist only two major S4 conformations, lacking intermediate ones. D540K mutation introduces additional intermediate S4 conformations, likely contributing to the U-shaped gating behavior. D540K/R665E restores the ‘all or none’ S4 movement in WT+ channels, further supporting our interpretation of a direct impact on S4 movement by D540K. This comparative analysis highlights the capability of FLIM phasor analysis in detecting potential intermediate conformations of the voltage sensor.

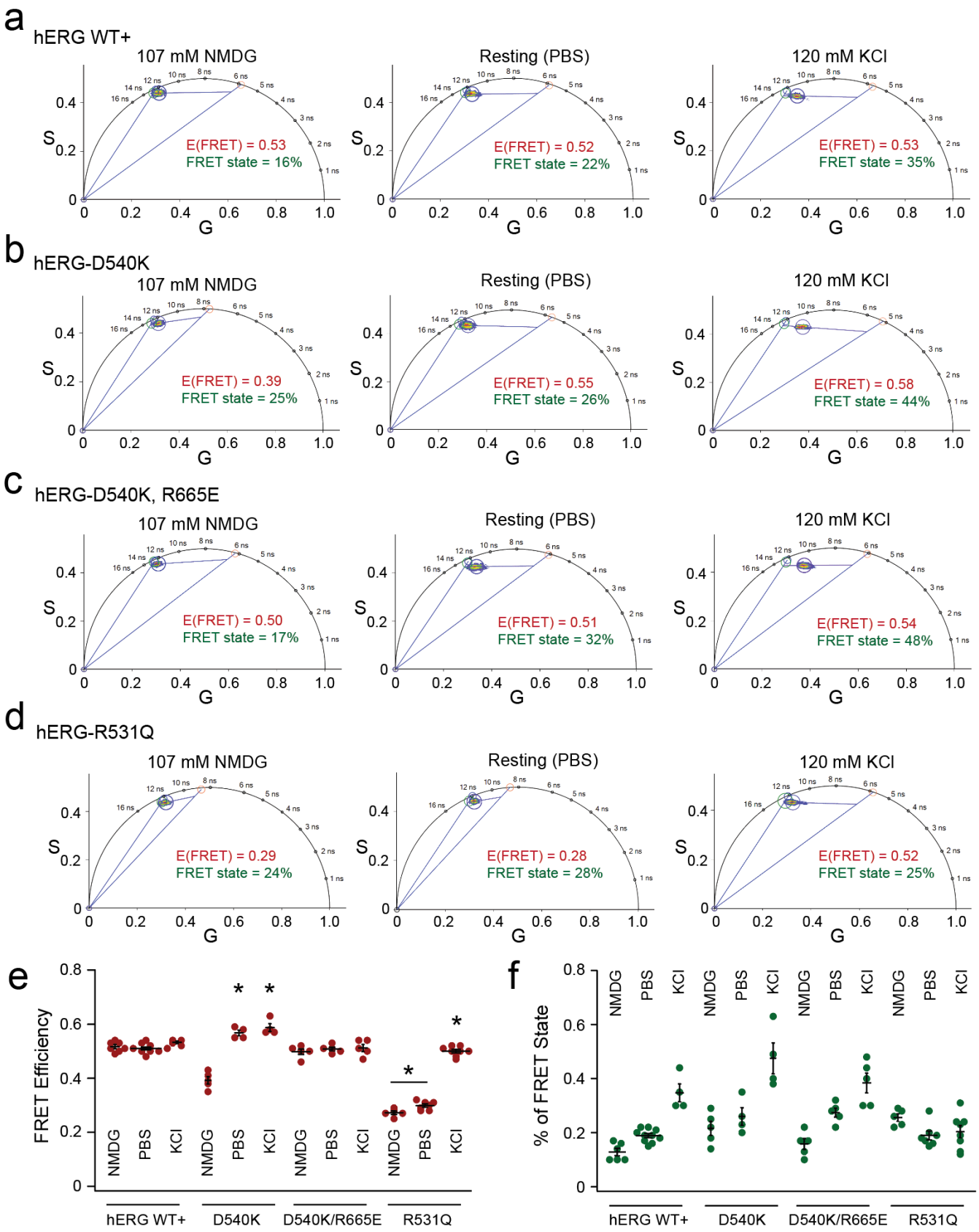
a
hERG WT+
107 mM NMDG
E(FRET) = 0.53
FRET state = 16%
Resting (PBS)
E(FRET) = 0.52
FRET state = 22%
120 mM KCl
E(FRET) = 0.53
FRET state = 35%
b
hERG-D540K
107 mM NMDG
E(FRET) = 0.39
FRET state = 25%
Resting (PBS)
E(FRET) = 0.55
FRET state = 26%
120 mM KCl
E(FRET) = 0.58
FRET state = 44%
c
hERG-D540K, R665E
107 mM NMDG
E(FRET) = 0.50
FRET state = 17%
Resting (PBS)
E(FRET) = 0.51
FRET state = 32%
120 mM KCl
E(FRET) = 0.54
FRET state = 48%
d
hERG-R531Q
107 mM NMDG
E(FRET) = 0.29
FRET state = 24%
Resting (PBS)
E(FRET) = 0.28
FRET state = 28%
120 mM KCl
E(FRET) = 0.52
FRET state = 25%
S
G
e
FRET Efficiency
NMDG
PBS
KCl
hERG WT+
D540K
D540K/R665E
R531Q
f
% of FRET State
NMDG
PBS
KCl
hERG WT+
D540K
D540K/R665E
R531Q

Fig. 3. Phasor linear unmixing analysis of FLIM-tmFRET in hERG channels under different voltage conditions.
a-d. Representative analysis of the L523/G439 tmFRET from individual cells for hERG WT+, hERG-D540K, hERG-D540K/R665E and hERG-R531Q channels under various conditions. **e-f**. Summary data of the estimated FRET efficiencies and percentage of the FRET state using linear unmixing of the phasor approach. Data shown are presented as mean ± s.e.m., n = 4 – 10. For FRET efficiencies of D540K, p = 6e-6 between NMDG and PBS conditions, p = 2e-6 between NMDG and KCl conditions. For the FRET efficiencies of R531Q, p = 0.03 between NMDG and PBS conditions, p = 3.5e-13 between NMDG and KCl conditions, and p = 3.8e-13 between PBS and KCl, one-way ANOVA (no adjustment).

Detecting intermediate voltage sensor states in hERG channels containing S4 mutations

Using the same FLIM-tmFRET L523/G439 pair in hERG, we tested the impact of the LQTS mutation R531Q on voltage sensor conformations (Fig. 3d). Our phasor analysis revealed at least two different FRET efficiencies: a lower one around 0.25 and a higher one similar to those observed in tmFRET experiments using the WT+ or with combined D540K/R665E mutations (Fig. 3 d-e). There was a notable prevalence of voltage sensors in the FRET state, even under more hyperpolarized voltages, with no increase upon membrane voltage elevation in our experimental conditions. Given the pronounced right shift in the G-V curve of hERG-R531Q channels, a more depolarized voltage (> +60 mV) might be necessary to observe an increase in the percentage of the FRET state. These findings suggest the presence of an intermediate conformation of the S4 voltage sensor induced by the R531Q mutation. At hyperpolarized voltages, the voltage sensor primarily transitions between the down and intermediate states relatively frequently (Fig. 3e, and percentage of FRET state = ~20%), while at more depolarized voltages, it can ascend to the up state. The measured donor-acceptor distance of 19 Å converted by the intermediate FRET efficiency (in comparison to 13 Å for the high FRET state) aligns with the intermediate conformation of VSD predicted by the cryo-EM structure of Eag channels[11].

To further validate the robustness of our method and test the hypothesis that R531Q produces additional intermediate conformational states of S4, we designed alternative FRET pairs. Using the same FRET donor site, L523TAG, we selected two additional acceptor sites: T436, and P440 (Fig. 4a). Both constructs, paired with L523TAG, exhibited noticeable membrane-localized YFP expression after employing the dual stop-codon suppression strategy. Compared to the L523/G439 FRET pair, the L523/P440 pair demonstrated lower FLIM-tmFRET efficiency, whereas the L523/T436 pair exhibited higher efficiencies (Fig. 4b). Including these two additional FRET pairs enabled us to examine the correlation between FRET efficiencies and Cβ-Cβ distances. A strong negative correlation was observed (r = -0.88) using a linear regression analysis (Fig. 4c). Moreover, similar to the FRET dynamics observed with the L523/G439 pair, only a single high-FRET state was detected, with the percentage of this state

adjustable by altering membrane voltage using external NMDG or 120 mM KCl (demonstrated with the L523/P440 pair in Fig. 4e-f). Collectively, these results indicate that: (1) the FLIM signals we measured predominantly originate from membrane-localized hERG-VSD; (2) the dual stop-codon suppression-mediated incorporation of Acd and ProK results in functional VSDs that respond to membrane potential changes; and (3) the phasor FLIM-FRET linear unmixing approach accurately predicts short-range interatomic distances between membrane helices in a native lipid environment. Moreover, the results obtained with the L523/P440 FRET pair in the presence of R531Q further support our conclusion that the R531Q mutation induces intermediate conformational states of the S4 helix in hERG channels (Fig. 4 e and f). The observation of intermediate FRET efficiencies under less depolarized membrane conditions (such as NMDG and PBS) aligns with the findings from the L523/G439 pair and reinforces the notion that this mutation leads to distinct voltage sensor conformations. Additionally, since the L523/T436 pair shared the same limitation as the previously mentioned L523/A430 pair, we opted not to test the effect of R531Q on potential intermediate FRET efficiencies for this pair.

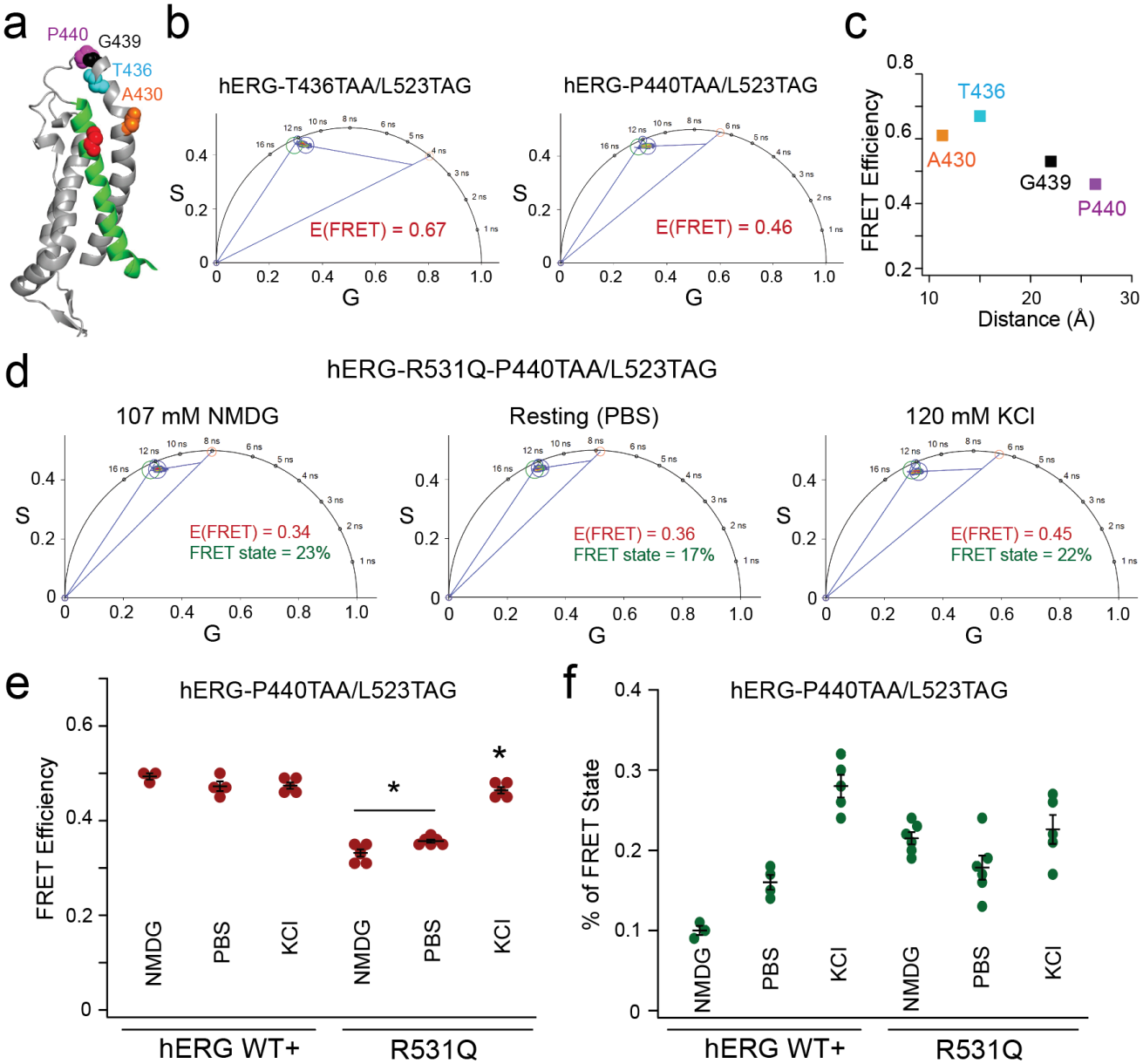

Fig. 4. Alternative tmFRET pairs yielded similar intermediate distances in the hERG-R531Q channel. **a**. Structural cartoon illustrating the four different tmFRET pairs, L523TAG as the donor and A430TAA, T436TAA, G439TAA, P440TAA as acceptors. **b**. Representative phasor analysis showing the different FRET efficiencies comparing the L523TAG/T436TAA and L523TAG/P440TAA pairs. Cells are imaged in the 120 mM KCl depolarizing condition. **c**. Relationship between the measured tmFRET efficiency in the depolarizing condition versus the β-carbon distance of FRET pairs. There is a trend that the degree of FRET is inversely correlated with the proximity of FRET pairs. **d**. Representative phasor-plot analysis of the L523/P440 tmFRET from individual cells for hERG WT+ (control) and hERGR531Q channels under various conditions. **e-f**. Summary data of the estimated FRET efficiencies and percentage of the FRET state using linear unmixing of the phasor approach. Data shown are presented as mean ± s.e.m., n = 3 – 6. For FRET efficiencies of R531Q, p = 0.025 between NMDG and PBS conditions, p = 1.3e-9 between NMDG and KCl conditions, and p = 2.1e-8 between PBS and KCl conditions, one-way ANOVA (no adjustment).

Similar intermediate state of the hERG S4 helix introduced by the R528Q mutation

We tested the presence of intermediate FRET states in hERG channels containing the R528Q mutation using the same tmFRET pair. As mentioned earlier, R528Q mutation induced biphasic channel activation, yet did not alter the G-V relationship compared to WT hERG channels (Supplementary Fig. 1d). Similar to the tmFRET results of R531Q mutant channels, phasor analysis revealed the presence of at least two different FRET efficiencies: a lower one around 0.35 (a converted distance of 16.6 Å) and a higher one around 0.5 (Fig. 5), suggesting that the intermediate state of S4 with R528Q likely resides in a slightly more elevated position compared to that of R531Q (Fig. 5e). Notably, unlike the R531Q mutant channels (as depicted in Fig. 4f compared with Fig. 5d), membrane depolarization increased the proportion of FRET states for R528Q-containing channels, indicating a higher probability of the S4 helix in the intermediate or the up states. This observation contrasts with the behavior observed in R531Q mutants and can be attributed to the more left shift in the G-V relationship observed in R528Q channels (Supplementary Fig. 1).

Additionally, we conducted parallel experiments on hERG channels containing the LQTS-related R534Q mutation (Supplementary Fig. 4). These experiments exhibited only a single high FRET state, distinct from the R528Q but similar to the WT+ channels, indicating an absence of S4 intermediate states (Supplementary Fig. 4). Together, our findings suggest that mutations affecting critical voltage-sensing arginines in hERG channels give rise to intermediate conformational states of the S4 helix. These intermediate states offer functional insights into interpreting the intermediate structures initially identified in Eag channels[11] and those proposed in other VGICs[12]. They suggest a novel mechanism through which LQTS-associated mutations can influence the gating of hERG channels and voltage sensing in cardiac tissue.

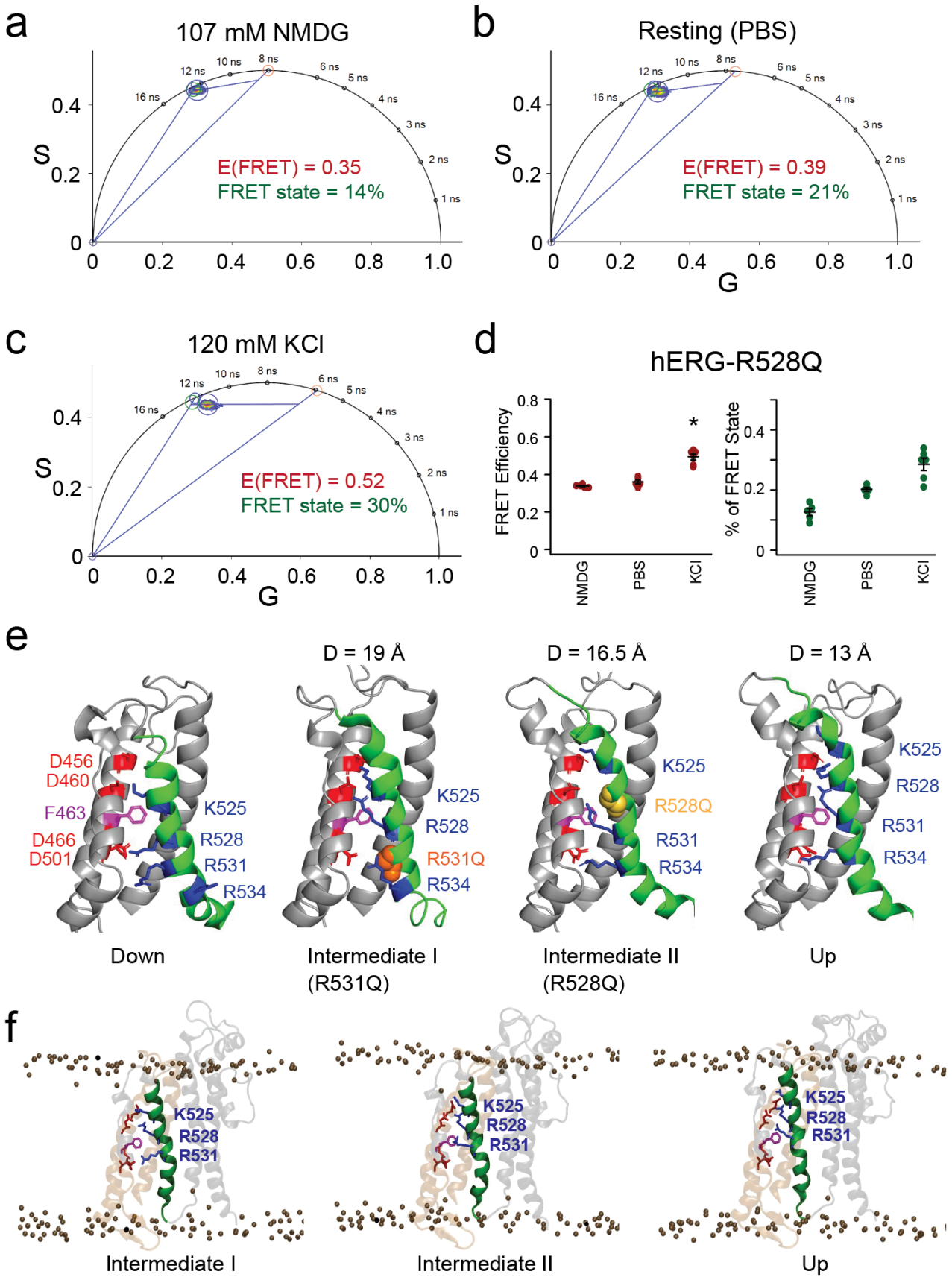
a
107 mM NMDG
E(FRET) = 0.35
FRET state = 14%
b
Resting (PBS)
E(FRET) = 0.39
FRET state = 21%
c
120 mM KCl
E(FRET) = 0.52
FRET state = 30%
d
hERG-R528Q
FRET Efficiency
% of FRET State
NMDG
PBS
KCl
e
D = 19 Å
D = 16.5 Å
D = 13 Å
D456
D460
F463
D466
D501
K525
R528
R531
R534
R531Q
R528Q
Down
Intermediate I
(R531Q)
Intermediate II
(R528Q)
Up
f
Intermediate I
Intermediate II
Up

Fig. 5. Distinct intermediate states induced by R531Q and R528Q, as suggested by tmFRET and SMD simulations.
a-c. Representative analysis of the L523/G439 tmFRET from individual cells, when R528Q was included. **d**. Summary data of the estimated FRET efficiencies and percentage of the FRET state using linear unmixing of the phasor approach. Data shown are presented as mean ± s.e.m., n = 5 – 6, p =1e-6 between NMDG and KCl conditions, and p = 8e-6 between PBS and KCl conditions, one-way ANOVA (no adjustment). **e**. Structural cartoons depict the hypothetical intermediate states I and II induced by the R531Q and R528Q mutations, respectively. These models are purely based on static and morph-generated structures derived from Eag cryo-EM structures. Additionally, negatively charged residues within the S3 and S4 helices are highlighted. Distances indicated are based on the tmFRET measurements between the L523/G439 FRET pair. **f**. The steered MD-generated conformations of the hERG VSD, providing structural information to the proposed intermediate VSD conformations. Membrane lipid head groups are shown as yellow spheres.

MD simulations suggest distinct VSD conformations caused by R531Q and R528Q

When a hERG channel tetramer, modeled based on the cryo-EM structure of the Eag channel in the down conformation, was relaxed in a native lipid environment at -150 mV using molecular dynamics (MD) simulations[46], we observed that the S4 helix adopted the down conformation in two out of the four VSDs. In the other two VSDs, however, it adopted an intermediate conformation, similar to the intermediate-state cryo-EM structure of Eag-channel VSD and the intermediate I state inferred from tmFRET results (Supplementary Fig. 6), providing initial MD-based evidence of this intermediate state. When we repeated the simulations at -150 mV and 0 mV for a monomeric hERG transmembrane domain, the VSD initially stabilized in the intermediate I conformation and was unstable in the down conformation. This suggests that cytosolic domains may play a role in stabilizing the down conformation in a tetrameric configuration, while the transmembrane domain alone favors the intermediate I state. Nevertheless, MD simulations of the transmembrane domain are computationally efficient, making them a practical choice for our subsequent simulations.

We also performed a nonequilibrium molecular dynamics (MD) simulation, specifically steered MD (SMD), to facilitate the transition of the S4 helix from intermediate conformation I to the up-state conformation at 0 mV, based on the cryo-EM structure of hERG channels (Fig. 5f and Supplementary Movie 1). As an SMD reference, we used the central positions of the K525, R528, and R531 side chains relative to the S2 helix as collective variables[47-49]. A 100 ns SMD simulation of a monomer containing only the transmembrane regions (S1-S6 helices) resulted in the expected upward displacement of the S4 segment, yielding an intermediate conformation resembling intermediate II, as inferred from tmFRET data (Supplementary Fig. 7). The S4 undergoes a modest up-down movement of approximately 5 Å, with the primary conformational change being the transition of R531 from below to above F463 in the charge transfer center. This feature of R531 aligns with the significantly greater functional impact of the R531Q

mutation compared to other arginine substitutions in S4. In addition, the modest scale of S4 movement is consistent with the relatively shallow G-V relationship of hERG channel activation. The simulated VSD trajectories provide insights into the movement of S4, helping to interpret our FLIM-FRET results. Presumably, R528Q and R531Q stabilize and trap the S4 in these intermediate states.

Since FRET efficiencies differed at hyperpolarized voltages (NMDG and resting) but were mostly similar at depolarized voltages (high KCl) among various hERG mutations, we simulated the relaxed VSD of unmutated hERG, R531Q, and R528Q at -150 mV in a lipid environment to identify potential structural differences (Fig. 6). To simplify the analysis, we modeled hERG monomers including only the S1–S6 helices, incorporating mutations. They mostly maintained the intermediate I conformation. Notably, in the R531Q mutant, the S4 helix was slightly elevated. The absence of the salt bridge due to R531Q in the lower half of S4 caused a tilt of the S4, leading to an upward displacement of the S5 helix (Fig. 6b and Supplementary Fig. 8). This displacement of S5 may induce a rearrangement of the pore-lining S6 helix, inhibiting pore opening. In the case of R528Q, a similar but less pronounced tilt of the S4 was observed, but neither the S4 nor the S5 exhibited noticeable upward motion compared to the WT (Fig. 6b and Supplementary Fig. 8). Additionally, at hyperpolarized -150 mV, R531Q altered the secondary structure of the S4, switching it from a predominantly α-helical configuration in the WT to a more pronounced 3_{10}-helical conformation. R528Q produced a similar effect in promoting the 3_{10}-helical conformation. These altered VSD conformations may underlie the intermediate FRET efficiencies detected in the mutants.

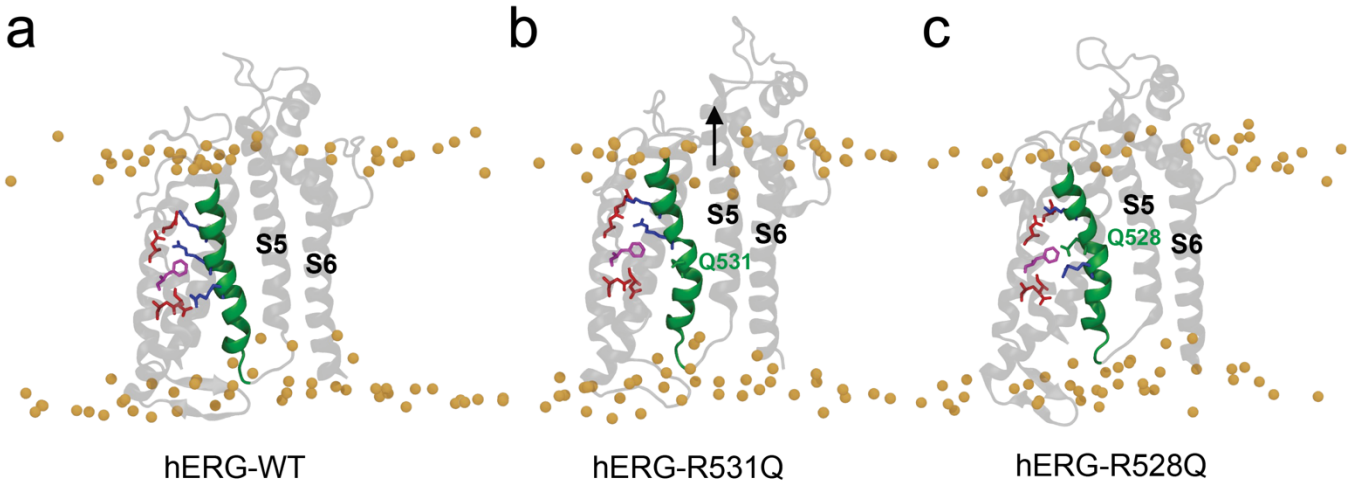

Fig. 6. MD simulations of the transmembrane regions of hERG revealed conformational changes induced by S4 arginine mutations.
a-c. MD-simulated conformations of the VSD monomer of hERG-WT (a), R531Q (b) and R528Q (c) mutants at hyperpolarized voltage (-150 mV). The arrow in panel b highlights the upward shift of the S5 helix caused by the R531Q.

DISCUSSION

Currently, there is a lack of effective methods for probing the conformational dynamics and heterogeneity of membrane proteins within living cells. While single-molecule FRET techniques offer substantial advantage in dissecting protein conformational states, their application in studying rapid and voltage-dependent events within native membranes remains challenging. Similarly, obstacles persist in employing methods such as cryo-EM and double electron-electron resonance (DEER), both of which routinely require cryogenic sample freezing. Fluorescence lifetime decays, similar to DEER decays, contain information that can be analyzed through multi-exponential functions, potentially unraveling distinct populations of fluorophores. Notably, these fluorescence lifetime techniques can be executed within native membranes and integrated with functional approaches like patch clamp. Leveraging a combination of genetic code expansion, click chemistry, frequency-domain phasor FLIM, and tmFRET, we engineered a live-cell system to measure intermediate states of ion channel voltage sensors in a relatively high-throughput manner. While the phasor FLIM technique has been used in quantifying multiple states of FRET in the field of cell biology[19], its potential in elucidating the structural biology of proteins is only beginning to be realized. This technique can be broadly applied to study protein dynamics, particularly for membrane proteins.

Building upon our findings, we postulate that neutralization of S4 positive charges gives rise to distinctive intermediate states within the S4 helix voltage sensor (Fig. 5e). Specifically, the negatively charged residues situated within the S2 and S3 helices, known as the extracellular negative cluster (ENC; D456 and D460) and intracellular negative cluster (INC; D466 and D501), play a role in stabilizing these intermediate states. In the case of R531Q mutation, the positively charged side chain of R528 is essential for S4 to interact with the ENC, thereby stabilizing its intermediate state. In contrast, in the instance of the R528Q mutation, S4 depends on the positive charge of the lower R531 to interact with the ENC, thereby resulting in an upward shift of its intermediate state, compared to that for the R531Q mutation (Fig. 5e). In other words, as the S4 moves upward, an intermediate state occurs when neutralized arginine side chains fail to exchange their ion pair partners as normal. Interestingly, the contrasting activation patterns observed between R531Q channels (long initial lag and mono-exponential activation) versus R528Q channels (short initial lag and double-exponential activation) may be due to the distinctive functional coupling of the intermediate II S4 conformation to channel opening. Stabilizing the intermediate II conformation may hinder pore closure, as evidenced by the significantly slower deactivation observed in the R528Q mutant. Conversely, stabilizing the intermediate I conformation could prevent pore opening. Furthermore, disrupting the characteristic "RXX" repeat, which governs arginine positioning, can bifurcate

the movement of the voltage sensor into distinct phases. This phenomenon is reminiscent of the biphasic S4 movement observed in the VSD of various other proteins and channels[50-53]. Moreover, the calculated probability of voltage sensors transitioning between distinct FRET states, using linear unmixing phasor analysis, can be calculated using Boltzmann's law to estimate the free energy associated with S4 voltage sensor activation[21,54]. Future investigations are needed to elucidate the impact of intermediate S4 conformations on the VSD-PD electromechanical coupling mechanisms underlying hERG channel gating. Finally, our results could provide insights to analogous S4-arginine (R2 and R3) mutations that cause cardiac diseases in other types of VGICs, e.g., in voltage-gated Na^+ channels[55-58].

Our MD simulations provide new insights into S4 movement in VGICs, particularly those in non-domain-swapped subunit arrangements, such as KCNH family channels[59,60]. The elevated S4 helix position induced by arginine mutations aligns with intermediate states predicted by FRET experiments. While some S4 arginine mutations generate gating pore currents in VGICs[61,62], R531Q produced little ionic current at hyperpolarized voltages. In non-domain-swapped VGICs, the closer proximity of S4 to S5 suggests that arginine mutations may have a greater impact on S5 and S6 in the pore domain than in domain-swapped VGICs[8,10,11,60]. Consequently, R531Q in hERG notably elevated the S5 position in our MD simulations. Additionally, it remains unclear whether a potential 3_{10}-helix to α-helix conversion modulates the intermediate state of voltage sensors[11,13,63,64]. In our SMD (Supplementary Movie 1), we noticed that during the upward movement of S4, the S4 regions transitioned from an α-helical to a 3_{10}-helical conformation while traversing the charge transfer center. This supports the idea that this arrangement allows the voltage-sensing arginines to align on one side of the helix with minimal rotation of S4. The observation that arginine mutations promote a 3_{10}-helical conformation at S4 down (or intermediate I) states suggests that such structural alterations could contribute to the functional changes, potentially by affecting the stability, movement, or energetics of the S4 in VGICs. Moreover, the tilt of the S4 caused by arginine mutations is reminiscent of similar motions observed in the S4 of non-domain-swapped VGICs, particularly in HCN channels[9,15,45,65]. This suggests that the C-terminal half of the S4 segment in this VGIC configuration is highly susceptible to tilting or bending motions, which plays a significant role in shaping the diversity of voltage-dependent gating mechanisms.

Our method represents a significant technical advance in the application of FLIM-FRET to structural biology in live-cell imaging experiments and shows promise for future improvement. Enhancing the selectivity of pyrrolysyl-tRNA synthetase for Acd is essential to minimize nonspecific fluorescence. The presence of endogenous genes using the amber codon might interfere with the Acd system, resulting in undesired cytosolic Acd fluorescence in our preparations. Developing an Acd variant that fluoresces

exclusively upon incorporation into the protein of interest would help mitigate the nonspecific Acd fluorescence as well. Furthermore, optimizing the linker length between ProK and azido DOTA could bring the transition metal acceptor closer to the protein backbone. This engineering can benefit from more efficient CuAAC click chemistry, requiring lower concentrations of Cu(I) catalyst and exhibiting faster reaction kinetics. Alternatively, engineering copper-free strain-promoted azide-alkyne cycloaddition (SPAAC) reactions could also facilitate labeling of the tmFRET acceptor[66,67]. Such improvements would not only enhance the accuracy of this method but also reduce the cytotoxicity associated with transition metals. Finally, incorporating patch clamp techniques into this method to precisely control membrane voltage could further enhance our ability to correlate channel function with structural states.

MATERIALS AND METHODS

Molecular Cloning

The bioorthogonal labeling of non-canonical amino acids (ncAAs) was achieved by site-specific incorporation using either single or dual codon suppression. This involved using amber (TAG) and ochre (TAA) codons within the channel protein of interest, specifically the hERG1 cDNAs synthesized by VectorBuilder (Chicago, IL). These constructs, featuring a C-terminal eYFP and a CMV promoter, were cloned and amplified using a mammalian gene expression vector. The S620T mutation, located in the pore helix of the channel, was included in all hERG1 constructs used in this study to eliminate rapid C-type inactivation[25-27]. This modification allows for a more accurate estimation of voltage-dependent activation by avoiding the overlap between activation and inactivation phases. Moreover, we believe that the S620T mutation does not impact the structure and function of the VSD. For simplicity, we refer to this modified hERG1-S620T channel as the 'WT+' channel throughout this paper.

DNA oligo primers, from Integrated DNA Technologies (IDT, Coralville, IA), were used for the design and synthesis process. Point mutations were induced using either the QuikChange II XL Site-Directed Mutagenesis or Multi Site-Directed Mutagenesis Kit (Agilent Technologies, Cedar Creek, TX). Subsequently, Dpn I restriction enzyme treatment (Agilent Technologies) was applied to digest the methylated parental DNA template of the DNA plasmids, which were then transformed into XL10-Gold competent cells (Agilent Technologies). The introduction of double functional stop codons opal (TGATGA) at the terminal end of YFP ensured successful translation termination. Verification of the introduced stop codons within the mutant plasmid was performed through DNA sequencing provided by either Genewiz (Azenta Life Sciences, Burlington, MA) or Plasmidsaurus (Eugene, OR). Additionally, the DNA concentration was quantified using a Nanodrop OneC spectrophotometer (Life Technologies, Grand Island, NY).

Cell Culture, Transient Transfection and Bioorthogonal Labeling

The tsA-201 cells, a variant of human embryonic kidney (HEK293) cells, were procured from Sigma-Aldrich (St. Louis, MO), authenticated via short tandem repeat (STR) profiling, and then cryopreserved in liquid nitrogen. For initiating new cell cultures, these cells were thawed and cultured in Dulbecco’s modified Eagle’s medium (DMEM; Gibco), supplemented with 10% fetal bovine serum (FBS;

Gibco) and 1% penicillin/streptomycin (Gibco), within a humidified incubator maintained at 37 °C with 5% CO_2.

Transfection was performed on 70% - 90% confluent tsA-201 cells using the lipofectamine 3000 kit (Invitrogen, Carlsbad, CA, #L30000080), following established protocols[68,69]. For dual stop-codon suppression, the cells were co-transfected with two plasmids: pAS_4xU6-PylT M15(UUA) FLAG-Mma PylRS (Mma PylT/RS) from Addgene (Watertown, MA, #154774)[34] and the Acd RS1 tRNA/aminoacyl-tRNA synthetase pair (GCE4All Research Center, Oregon State University)[33], along with a third plasmid containing the dual stop-codon mutations (TAG and TAA) of the hERG gene required for selective incorporation of two noncanonical amino acids (ncAAs): Acd (the Petersson Lab, University of Pennsylvania) and N-propargyl-L-lysine (ProK) (SiChem, Bremen, Germany)[34]. This Acd RS1 tRNA/aminoacyl-tRNA synthetase pair consists of one copy of aminoacyl-tRNA synthetase and four copies of tRNA. To facilitate nonsense suppression, a human dominant-negative release factor eRF1 (E55D) (VectorBuilder, Chicago, IL) was co-transfected[70]. The ncAAs were added to the transfection solution: 5 μM Acd and 0.25 mM ProK. ProK was mixed with 1 M HEPES solution in a 1:4 ratio (Sigma-Aldrich, St. Louis, MO) before adding to cell culture. The ProK stock solution (100 mM) were made by dissolving ProK in 0.2 M NaOH water. In the absence of the pAS_4xU6-PylT M15(UUA) FLAG-Mma PylRS (Mma PylT/RS) while in the presence of the Acd incorporation system, we did not observe significant membrane-localized YFP signals (Supplementary Fig. 2f), indicating the Acd RS1 tRNA/aminoacyl-tRNA synthetase pair is specific to the amber stop codon and cannot suppress the ochre stop codon.

At the ProK site, we conducted the copper-catalyzed azide-alkyne cycloaddition (CuAAC) reaction using 50 μM $CuSO_4$, 250 μM THPTA (Tris(benzyltriazolylmethyl)amine), and 2.5 mM ascorbic acid in DMEM medium[34]. For azido-DOTA labeling (at 100 μM in cell culture), the incubation proceeded for 1-1.5 hours at 37 °C. To produce Cu^{2+}-DOTA, we mixed equal amounts of 100 mM DOTA azide stock and 110 mM $CuSO_4$ stock, allowing them to incubate for five minutes until the mixture transitioned from light to darker blue, indicating Cu^{2+} binding to DOTA. Once bound, DOTA and Cu^{2+} dissociation occurred very slowly due to their picomolar affinity[31]. The azido-mono-amide-DOTA was purchased from Macrocyclics, Inc (Plano, TX).

Fluorescence Microscopy, Fluorescence Lifetime measurement and FLIM-FRET

Fluorescence measurements were conducted using an Olympus IX73 inverted microscope (Olympus America, Waltham, MA), equipped with a 60× U Plan S-Apo 1.2-NA water-immersion objective. Epifluorescence recording was facilitated by wide-field excitation from a pE-800 LED light source (CoolLED, Andover, UK). For choosing cells with strong membrane localized YFP fluorescence via eyepiece of the microscope, YFP was excited using a 500 nm LED line. Acd fluorescence was expected in these cells and was excited using a 365 nm LED line. The imaging solution used for cell visualization was Dulbecco's phosphate-buffered saline (PBS, ThermoFisher), unless specified otherwise. All microscopic experiments were conducted at room temperature.

Spectral measurements of Acd fluorescence used a spectrograph (SpectroPro 2156, 300 groves/mm grating, 500 nm blaze; Teledyne Princeton Instruments, Acton, MA) situated between the microscope output port and an INFINITY3S-1URM CCD camera (Teledyne Lumenera, Ottawa, ON). Acd fluorescence from cells was excited using a 365 nm LED line through a filter cube. The emission filter was removed from the filter cube, allowing only fluorescence in the wavelength range of 423 to 597 nm collected as a spectral image. Spectral images were acquired with exposure times of 500 ms. In addition, spectral measurements of the light absorption of transition metals were made using the Nanodrop OneC spectrophotometer (Life Technologies, Grand Island, NY). Subsequent analysis of the spectral data was conducted using ImageJ/Fiji (National Institutes of Health, USA) and Igor Pro 9 (Wavemetrics, Portland, OR).

Digital frequency-domain fluorescence lifetime imaging was conducted using a Q2 laser scanning confocal system, which was equipped with a FastFLIM data acquisition module (ISS, Inc, Champaign, IL) and two hybrid PMT detectors (Model R10467-40, Hamamatsu USA, Bridgewater, NJ), as previously described[18,31,71]. This confocal FLIM system is integrated with the Olympus IX73 inverted microscope. The fluorescence lifetime measurements encompass both frequency-domain (allowing instantaneous distortion-free phasor plotting) and time-domain decay information. To excite Acd, a 375 nm pulsed diode laser (ISS, Inc) controlled by FastFLIM was used, with the emitted fluorescence captured through a 447/60 nm band-pass emission filter. YFP excitation was achieved using a 488 nm wavelength excitation and collected through a 542/27 nm emission filter. Simultaneous two-color imaging was facilitated by dichroic cubes, with one containing a 50/50 beam splitter and the other equipped with long-pass filters.

For image acquisition, confocal images with a frame size of 256 x 256 pixels were obtained for each experimental condition, using a motorized variable pinhole (set at a size of 100 μm). To determine the phase delays (φ) and modulation ratios (m) of the fluorescence signal in response to an oscillatory

stimulus (6 ps per pulse) with a frequency ω = 20 MHz, the VistaVision software (ISS, Inc) associated with the FastFLIM system was used. These values were obtained by performing sine and cosine Fourier transforms of the phase histogram, taking into account the instrument response function (IRF) calibrated with Atto 425 in water (with a lifetime of 3.6 ns, see Supplementary Fig. 2). VistaVision software, equipped with the imaging and FLIM module, was also used for image processing, display, and acquisition. This software allowed for the specification of parameters such as pixel dwell time, region of interest, and resolution. Additionally, it employed a fitting algorithm, phasor linear unmixing analysis for FLIM-tmFRET analysis. To enhance display and analysis of membrane-localized lifetime species, a median/gaussian smoothing filter and an intensity-based selection of the membrane region were applied. The VistaVision and phasor FLIM provide a significant advantage by effectively differentiating signals originating from background and cytosolic fluorescence outside the membrane region from those within the plasma membrane. This capability is especially important given that our Acd incorporation system tends to generate substantial nonspecific cytosolic fluorescence, which constitutes the primary error source in our experiments. Relying on the selection of cells exhibiting membrane-localized YFP fluorescence enabled us to analyze lifetime species of the Acd fluorescence mostly aligned with YFP fluorescence locations (Supplementary Fig. 2). The exact reason for the greater cytosolic Acd fluorescence comparing to other systems that incorporate fluorescent noncanonical amino acids (e.g. L-Anap) via stop-codon suppression is unclear[31,33,38,72], and likely due to the high membrane permeability of Acd and nonspecific amber stop-codon suppression of endogenous genes. Additionally, we engineered a similar plasmid containing the Acd RS1 tRNA/aminoacyl-tRNA synthetase pair with one copy of aminoacyl-tRNA synthetase but only two copies of tRNA, which was sufficient to achieve dual-stop-codon suppression, indicated by significant membrane-localized YFP fluorescence. However, this modification did not reduce the nonspecific cytosolic Acd fluorescence.

The VistaVision software features the FRET trajectory function to estimate the FRET efficiency, manifesting an averaged distance between donor and acceptor probes. As previously described, key parameters are adjusted to optimize the fitting trajectory through both the donor alone and the donor species due to quenching by FRET acceptors[31]. Regarding the linear unmixing (decomposition) approach of calculating FRET efficiency, the linear fitting process underwent visual inspection to derive four parameters: (1) background contribution in the donor-alone (or low FRET) sample, (2) background contribution in the donor sample in the presence of the acceptor, (3) percentage contribution by the FRET state, and (4) FRET efficiency under theoretical conditions where 100% donors undergo high FRET. Background levels typically remained at or below 5%, consistent with the minimal emission intensity observed in untransfected cells. To determine the percentage contribution by the FRET state, the cursor

position was adjusted to cover the central portion of the lifetime distribution. The FRET efficiency of the low FRET state corresponding to the down state of the S4 cannot be accurately measured since the lifetime species typically would not exhibit an oval-shaped distribution and localize very close to those of the donor alone in the phasor plot.

The distances *r* between the Acd and Cu^{2+}-DOTA acceptors were estimated using the convolution of the Förster equation ($E_{max.} = 1 / (1 + (r / R_0)^6)$) with a Gaussian function: Förster convolved Gaussian (FCG) as previously established[9,72]. The FCG adopts a Gaussian distribution with a standard deviation (σ) of 7.5 Å and a full width at half maximum (FWHM) of 17.7 Å (Supplementary Fig. 5). This assumption was based on the interatomic distance distribution of probes with similar labels, e.g., the L-Anap and Cu^{2+}-TETAC tmFRET pair[9,21,72]. The R_0 value was calculated using the following equation:

$$\mathrm{R}_0 = \mathrm{C}\sqrt[6]{JQ\eta^{-4}\kappa^2} \qquad (1)$$

where *C* is the scaling factor, *J* is the overlap integral of the Anap emission spectrum and the YFP absorption spectrum, Q is the quantum yield of the Acd (around 0.8), η is the index of refraction, and κ^2 is the orientation factor. η was assumed to be 1.33, and κ^2 was assumed to be 2/3. This calculation generated a R_0 of 13 Å between Acd and Cu^{2+}-DOTA and 12 Å between Acd and Co^{2+}-DOTA. Our FRET distance calculation aimed to provide a quantitative description of conformational heterogeneity rather than to precisely define the magnitude of S4 movement.

Patch-Clamp Electrophysiology

Whole-cell patch-clamp recordings were conducted at a temperature range of 22 - 24 °C using an EPC10 patch-clamp amplifier and PATCHMASTER (HEKA) software. Borosilicate patch electrodes, with an initial pipette resistance of approximately 3 - 5 MΩ, were fabricated using a P1000 micropipette puller from Sutter Instrument (Sutter, Novato, CA). Current signals were low-pass filtered and sampled at a frequency of 10 kHz. Series resistance was mostly under 10 MΩ and compensated at ~ 40-70%. Patch clamp was performed using a Sutter MP-225A motorized micromanipulator (Sutter, Novato, CA).

To record hERG currents from tsA-201 cells, the internal pipette solution was prepared with the following composition (in mM): 10 NaCl, 130 KCl, 3 $MgCl_2$, 10 HEPES, 0.5 EGTA, 1 MgATP, 0.3 Na_3GTP, and pH 7.2 adjusted with KOH. The external solution used was Ringer's solution with the following composition (in mM): 160 NaCl, 2.5 KCl, 1 $MgCl_2$, 2 $CaCl_2$, 10 HEPES, 8 D-Glucose, and pH 7.4 adjusted

with NaOH. 10 mM TEA was added to the external solution to block endogenous potassium currents of tsA cells, while having minor effect on the hERG currents[24]. For hyperpolarizing and depolarizing solutions, 107 mM impermeant cation NMDG (N-methyl-D-glucamine) and 120 mM KCl replaced NaCl in the Ringer's solution, respectively[41].

The conductance-voltage (G-V) relationships were determined by analyzing the instantaneous tail currents subsequent to voltage pulse steps. Subtraction of leak tail currents was performed, and the resulting currents were normalized to the maximum tail current amplitude (G/G_{max}). The relative conductance was then plotted against the voltage of the main pulse and fitted using the Boltzmann equation:

$$G/G_{max}=1/(1 + exp[(V_{1/2} - V)/Vs]) \qquad (2)$$

where V is the membrane potential, $V_{1/2}$ is the potential for half-maximal activation, and Vs is the slope factor.

Modeling hERG VSD states

Our initial hERG-VSD model was constructed through homology modeling, using the cryo-EM structure of the VSD in the down state of an Eag channel as a template[11]. The homology model was embedded in a membrane representative of the sarcolemma, with the following lipid composition: PC (33%), PS (3.5%), PE (17%), PIP_2 (3.5%), cholesterol (33%), and sphingomyelin (10%)[73]. The system was solvated in 0.15 M KCl using the TIP3P water model within a 205 Å x 205 Å x 190 Å unit cell[74]; the final assembly consists of 720k atoms. After equilibration, the system was simulated under an applied potential of -150 mV for 1 μs.

All MD simulations in this study were conducted using NAMD3 with a 2 fs timestep[75,76]. The systems were equilibrated under the NPT ensemble, maintaining the temperature at 310 K with the Langevin thermostat[77]. The Nosé–Hoover Langevin piston method was used to keep the pressure at 1 bar, and τ_p = 0.1 ps for 50 ns[78,79]. Particle mesh Ewald (PME)[80] summation was used for long-range electrostatic interactions, with a 12 Å cutoff, and a 10 Å switching distance was applied for van der Waals interactions.

Steered Molecular Dynamics (SMD) Simulations

For SMD simulations, a transmembrane domain (TMD), residues 405 - 667, of a single monomer from hERG down state was embedded in a membrane, with the same composition as the equilibrium simulations described above and solvated in 0.15 M KCl using TIP3P water; the resulting system size was 150 Å x 150 Å x 130 Å; the total system size was 255k atoms. This TMD was initially simulated under the applied voltage of -150 mV to obtain a relaxed starting model, resembling the intermediate I state. SMD was then used to steer it to the VSD up state at 0 mV using three “distance Z” collective variables; the three collective variables were defined as the vertical displacement from the center of mass (COM) of K525, R528, and R531 sidechain atoms, with respect to the COM for the S2 helix backbone atoms. The target value for these variables was defined with respect to the structure of hERG, in the VSD up state captured by cryo-EM (PDB: 5VA1)[81]. Specifically, for SMD of the WT TMD, the distance values were 7.6 Å for K525, 3.0 Å for R528, -5.4 Å for R531 in the starting model, to 11.4 Å for K525, 6.3 Å for R528, and 0.9 Å for R531 in the up state. The S1-S3 helices were restrained along the z-axis (membrane normal) with 10 kcal/mol/Å^2 harmonic restraints. Simultaneously, a pulling force was applied to each collective variable using a harmonic potential with a spring constant of 90 kcal/mol/Å^2. The SMD simulation was performed over 100 ns.

Statistics and Reproducibility

Statistical significance was assessed based on data parameters presented as the mean ± s.e.m. of n independent cells or patches. The two-sided Student’s t-test was used for comparing two groups, while a one-way ANOVA followed by Tukey's post hoc test was employed for pairwise comparisons involving more than two data groups.

DATA AVAILABILITY

Source data are available as a Source Data file in figshare.com, doi:10.6084/m9.figshare.28304378, and additional data are in the Supplementary Information.

CODE AVAILABILITY

Computational codes and models are available in figshare.com, doi:10.6084/m9.figshare.28304378.

ACKNOWLEGEMENT

We thank Natalie L. Macchi for technical support; Joel C. Eissenberg for editing the manuscript; Enrico Di Cera and Nicola Pozzi for feedback, E. James Petersson and Venkatesh Yarra (University of Pennsylvania) for sharing the noncanonical amino acid Acd and providing advice; Ryan A. Mehl (GCE4All Research Center, Oregon State University) for sharing the Acd RS1 aminoacyl tRNA synthetase and tRNA pair plasmid. This research is supported by startup funds from the Edward A. Doisy Department of Biochemistry and Molecular Biology, Saint Louis University School of Medicine (to G.D.), and by National Institutes of Health (NIH) grants R35GM154778 (to G.D.) and R56HL169176 (to G.D. and E.T.). In addition, the authors acknowledge funding from the NIH grant R24-GM145965 (to E.T.) and National Science Foundation (NSF) QCB grant: 221835 (to E.T.). Computing resources were provided by the NSF ACCESS award: MCA06N060 (to E.T.).

AUTHOR CONTRIBUTIONS

G.D. conceived and designed the research. G.D. performed and analyzed fluorescence imaging experiments. L.J.H. performed patch-clamp recordings. L.J.H. and G.D. analyzed patch-clamp data. E.N.L. and G.D. performed molecular cloning of mutant hERG constructs. A.N.C, E.T. and G.D. designed MD simulations. A.N.C. performed and analyzed MD simulations. G.D. wrote the manuscript with inputs from A.N.C and E.T..

COMPETING INTERESTS

The authors declare no competing interests.

REFERENCES

1 Hille, B. *Ion Channels of Excitable Membranes* 3rd edn, (Sinauer Associates, 2001).

2 Catterall, W. A., Wisedchaisri, G. & Zheng, N. The chemical basis for electrical signaling. *Nat Chem Biol* **13**, 455-463 (2017). https://doi.org:10.1038/nchembio.2353

3 Trudeau, M. C., Warmke, J. W., Ganetzky, B. & Robertson, G. A. HERG, a human inward rectifier in the voltage-gated potassium channel family. *Science* **269**, 92-95 (1995).

4 Ganetzky, B., Robertson, G. A., Wilson, G. F., Trudeau, M. C. & Titus, S. A. The eag family of K^+ channels in Drosophila and mammals. *Ann N Y Acad Sci* **868**, 356-369 (1999).

5 Anderson, C. L. *et al.* Large-scale mutational analysis of Kv11.1 reveals molecular insights into type 2 long QT syndrome. *Nat Commun* **5**, 5535 (2014). https://doi.org:10.1038/ncomms6535

6 Guo, J. *et al.* Structure of the voltage-gated two-pore channel TPC1 from Arabidopsis thaliana. *Nature* **531**, 196-201 (2016). https://doi.org:10.1038/nature16446

7 Xu, H. *et al.* Structural Basis of Nav1.7 Inhibition by a Gating-Modifier Spider Toxin. *Cell* **176**, 1238-1239 (2019). https://doi.org:10.1016/j.cell.2019.01.047

8 Wisedchaisri, G. *et al.* Resting-State Structure and Gating Mechanism of a Voltage-Gated Sodium Channel. *Cell* (2019). https://doi.org:10.1016/j.cell.2019.06.031

9 Dai, G., Aman, T. K., DiMaio, F. & Zagotta, W. N. The HCN channel voltage sensor undergoes a large downward motion during hyperpolarization. *Nat Struct Mol Biol* **26**, 686-694 (2019). https://doi.org:10.1038/s41594-019-0259-1

10 Dai, G., Aman, T. K., DiMaio, F. & Zagotta, W. N. Electromechanical coupling mechanism for activation and inactivation of an HCN channel. *Nat Commun* **12**, 2802 (2021). https://doi.org:10.1038/s41467-021-23062-7

11 Mandala, V. S. & MacKinnon, R. Voltage-sensor movements in the Eag Kv channel under an applied electric field. *Proc Natl Acad Sci U S A* **119**, e2214151119 (2022). https://doi.org:10.1073/pnas.2214151119

12 Mandala, V. S. & MacKinnon, R. The membrane electric field regulates the PIP_2-binding site to gate the KCNQ1 channel. *Proc Natl Acad Sci U S A* **120**, e2301985120 (2023). https://doi.org:10.1073/pnas.2301985120

13 Long, S. B., Campbell, E. B. & Mackinnon, R. Voltage sensor of Kv1.2: structural basis of electromechanical coupling. *Science* **309**, 903-908 (2005). https://doi.org:10.1126/science.1116270

14 Long, S. B., Tao, X., Campbell, E. B. & MacKinnon, R. Atomic structure of a voltage-dependent K^+ channel in a lipid membrane-like environment. *Nature* **450**, 376-382 (2007). https://doi.org:10.1038/nature06265

15 Lee, C. H. & MacKinnon, R. Voltage Sensor Movements during Hyperpolarization in the HCN Channel. *Cell* **179**, 1582-1589 e1587 (2019). https://doi.org:10.1016/j.cell.2019.11.006

16 Han, S. *et al.* Cholesterol inhibits human voltage-gated proton channel hHv1. *Proc Natl Acad Sci U S A* **119**, e2205420119 (2022). https://doi.org:10.1073/pnas.2205420119

17 Han, S. *et al.* Structural dynamics determine voltage and pH gating in human voltage-gated proton channel. *Elife* **11** (2022). https://doi.org:10.7554/eLife.73093

18 Digman, M. A., Caiolfa, V. R., Zamai, M. & Gratton, E. The phasor approach to fluorescence lifetime imaging analysis. *Biophys J* **94**, L14-16 (2008). https://doi.org:10.1529/biophysj.107.120154

19 Hinde, E., Digman, M. A., Hahn, K. M. & Gratton, E. Millisecond spatiotemporal dynamics of FRET biosensors by the pair correlation function and the phasor approach to FLIM. *Proc Natl Acad Sci U S A* **110**, 135-140 (2013). https://doi.org:10.1073/pnas.1211882110

20 Zagotta, W. N. *et al.* An improved fluorescent noncanonical amino acid for measuring conformational distributions using time-resolved transition metal ion FRET. *Elife* **10** (2021). https://doi.org:10.7554/eLife.70236

21 Zagotta, W. N. *et al.* Measuring conformational equilibria in allosteric proteins with time-resolved tmFRET. *Biophys J* (2024). https://doi.org:10.1016/j.bpj.2024.01.033
22 McBride, C. M. *et al.* Mechanistic basis for type 2 long QT syndrome caused by KCNH2 mutations that disrupt conserved arginine residues in the voltage sensor. *J Membr Biol* **246**, 355-364 (2013). https://doi.org:10.1007/s00232-013-9539-6
23 Waterhouse, A. *et al.* SWISS-MODEL: homology modelling of protein structures and complexes. *Nucleic Acids Res* **46**, W296-W303 (2018). https://doi.org:10.1093/nar/gky427
24 Choi, K. H., Song, C., Shin, D. & Park, S. hERG channel blockade by externally applied quaternary ammonium derivatives. *Biochim Biophys Acta* **1808**, 1560-1566 (2011). https://doi.org:10.1016/j.bbamem.2011.02.008
25 Codding, S. J. & Trudeau, M. C. The hERG potassium channel intrinsic ligand regulates N- and C-terminal interactions and channel closure. *J Gen Physiol* **151**, 478-488 (2019). https://doi.org:10.1085/jgp.201812129
26 Herzberg, I. M., Trudeau, M. C. & Robertson, G. A. Transfer of rapid inactivation and sensitivity to the class III antiarrhythmic drug E-4031 from HERG to M-eag channels. *J Physiol* **511 (Pt 1)**, 3-14 (1998). https://doi.org:10.1111/j.1469-7793.1998.003bi.x
27 Lau, C. H. Y. *et al.* Potassium dependent structural changes in the selectivity filter of HERG potassium channels. *Nat Commun* **15**, 7470 (2024). https://doi.org:10.1038/s41467-024-51208-w
28 Zhang, M., Liu, J. & Tseng, G. N. Gating charges in the activation and inactivation processes of the HERG channel. *J Gen Physiol* **124**, 703-718 (2004). https://doi.org:10.1085/jgp.200409119
29 Aggarwal, S. K. & MacKinnon, R. Contribution of the S4 segment to gating charge in the Shaker K^+ channel. *Neuron* **16**, 1169-1177 (1996). https://doi.org:10.1016/s0896-6273(00)80143-9
30 Zagotta, W. N., Hoshi, T., Dittman, J. & Aldrich, R. W. Shaker potassium channel gating. II: Transitions in the activation pathway. *J Gen Physiol* **103**, 279-319 (1994). https://doi.org:10.1085/jgp.103.2.279
31 Handlin, L. J. & Dai, G. Direct regulation of the voltage sensor of HCN channels by membrane lipid compartmentalization. *Nat Commun* **14**, 6595 (2023). https://doi.org:10.1038/s41467-023-42363-7
32 Jones, C. M. *et al.* Genetic encoding of a highly photostable, long lifetime fluorescent amino acid for imaging in mammalian cells. *Chem Sci* **12**, 11955-11964 (2021). https://doi.org:10.1039/d1sc01914g
33 Avila-Crump, S. *et al.* Generating Efficient Methanomethylophilus alvus Pyrrolysyl-tRNA Synthetases for Structurally Diverse Non-Canonical Amino Acids. *ACS Chem Biol* **17**, 3458-3469 (2022). https://doi.org:10.1021/acschembio.2c00639
34 Meineke, B., Heimgartner, J., Eirich, J., Landreh, M. & Elsasser, S. J. Site-Specific Incorporation of Two ncAAs for Two-Color Bioorthogonal Labeling and Crosslinking of Proteins on Live Mammalian Cells. *Cell Rep* **31**, 107811 (2020). https://doi.org:10.1016/j.celrep.2020.107811
35 Horrocks, W. D., Jr., Holmquist, B. & Vallee, B. L. Energy transfer between terbium (III) and cobalt (II) in thermolysin: a new class of metal--metal distance probes. *Proc Natl Acad Sci U S A* **72**, 4764-4768 (1975).
36 Taraska, J. W., Puljung, M. C., Olivier, N. B., Flynn, G. E. & Zagotta, W. N. Mapping the structure and conformational movements of proteins with transition metal ion FRET. *Nat Methods* **6**, 532-537 (2009). https://doi.org:10.1038/nmeth.1341
37 Zagotta, W. N., Gordon, M. T., Senning, E. N., Munari, M. A. & Gordon, S. E. Measuring distances between TRPV1 and the plasma membrane using a noncanonical amino acid and transition metal ion FRET. *J Gen Physiol* **147**, 201-216 (2016). https://doi.org:10.1085/jgp.201511531
38 Dai, G. & Zagotta, W. N. Molecular mechanism of voltage-dependent potentiation of KCNH potassium channels. *Elife* **6** (2017). https://doi.org:10.7554/eLife.26355

39 Malacrida, L., Ranjit, S., Jameson, D. M. & Gratton, E. The Phasor Plot: A Universal Circle to Advance Fluorescence Lifetime Analysis and Interpretation. *Annu Rev Biophys* **50**, 575-593 (2021). https://doi.org:10.1146/annurev-biophys-062920-063631
40 Ranjit, S., Malacrida, L., Jameson, D. M. & Gratton, E. Fit-free analysis of fluorescence lifetime imaging data using the phasor approach. *Nat Protoc* **13**, 1979-2004 (2018). https://doi.org:10.1038/s41596-018-0026-5
41 Kucka, M. *et al.* Dependence of multidrug resistance protein-mediated cyclic nucleotide efflux on the background sodium conductance. *Mol Pharmacol* **77**, 270-279 (2010). https://doi.org:10.1124/mol.109.059386
42 Vallmitjana, A. *et al.* Resolution of 4 components in the same pixel in FLIM images using the phasor approach. *Methods Appl Fluoresc* **8**, 035001 (2020). https://doi.org:10.1088/2050-6120/ab8570
43 Vallmitjana, A., Torrado, B., Dvornikov, A., Ranjit, S. & Gratton, E. Blind Resolution of Lifetime Components in Individual Pixels of Fluorescence Lifetime Images Using the Phasor Approach. *J Phys Chem B* **124**, 10126-10137 (2020). https://doi.org:10.1021/acs.jpcb.0c06946
44 Tristani-Firouzi, M., Chen, J. & Sanguinetti, M. C. Interactions between S4-S5 linker and S6 transmembrane domain modulate gating of HERG K+ channels. *J Biol Chem* **277**, 18994-19000 (2002). https://doi.org:10.1074/jbc.M200410200
45 Kasimova, M. A. *et al.* Helix breaking transition in the S4 of HCN channel is critical for hyperpolarization-dependent gating. *Elife* **8** (2019). https://doi.org:10.7554/eLife.53400
46 Roux, B. The membrane potential and its representation by a constant electric field in computer simulations. *Biophys J* **95**, 4205-4216 (2008). https://doi.org:10.1529/biophysj.108.136499
47 Moradi, M. & Tajkhorshid, E. Mechanistic picture for conformational transition of a membrane transporter at atomic resolution. *Proc Natl Acad Sci U S A* **110**, 18916-18921 (2013). https://doi.org:10.1073/pnas.1313202110
48 Moradi, M. & Tajkhorshid, E. Computational Recipe for Efficient Description of Large-Scale Conformational Changes in Biomolecular Systems. *J Chem Theory Comput* **10**, 2866-2880 (2014). https://doi.org:10.1021/ct5002285
49 Moradi, M., Enkavi, G. & Tajkhorshid, E. Atomic-level characterization of transport cycle thermodynamics in the glycerol-3-phosphate:phosphate antiporter. *Nat Commun* **6**, 8393 (2015). https://doi.org:10.1038/ncomms9393
50 Villalba-Galea, C. A., Sandtner, W., Starace, D. M. & Bezanilla, F. S4-based voltage sensors have three major conformations. *Proc Natl Acad Sci U S A* **105**, 17600-17607 (2008). https://doi.org:10.1073/pnas.0807387105
51 Lacroix, J. J. *et al.* Intermediate state trapping of a voltage sensor. *J Gen Physiol* **140**, 635-652 (2012). https://doi.org:10.1085/jgp.201210827
52 Dickinson, M. S. *et al.* Molecular basis of multistep voltage activation in plant two-pore channel 1. *Proc Natl Acad Sci U S A* **119** (2022). https://doi.org:10.1073/pnas.2110936119
53 Wu, X., Ramentol, R., Perez, M. E., Noskov, S. Y. & Larsson, H. P. A second S4 movement opens hyperpolarization-activated HCN channels. *Proc Natl Acad Sci U S A* **118** (2021). https://doi.org:10.1073/pnas.2102036118
54 Eggan, P., Gordon, S. E. & Zagotta, W. N. Ligand-coupled conformational changes in a cyclic nucleotide-gated ion channel revealed by time-resolved transition metal ion FRET. *Elife* **13** (2024). https://doi.org:10.7554/eLife.99854
55 Moreau, A., Gosselin-Badaroudine, P., Boutjdir, M. & Chahine, M. Mutations in the Voltage Sensors of Domains I and II of Nav1.5 that are Associated with Arrhythmias and Dilated Cardiomyopathy Generate Gating Pore Currents. *Front Pharmacol* **6**, 301 (2015). https://doi.org:10.3389/fphar.2015.00301
56 Daniel, L. L. *et al.* SCN5A variant R222Q generated abnormal changes in cardiac sodium current and action potentials in murine myocytes and Purkinje cells. *Heart Rhythm* **16**, 1676-1685 (2019). https://doi.org:10.1016/j.hrthm.2019.05.017

57 Moreau, A. *et al.* A leaky voltage sensor domain of cardiac sodium channels causes arrhythmias associated with dilated cardiomyopathy. *Sci Rep* **8**, 13804 (2018). https://doi.org:10.1038/s41598-018-31772-0
58 Calloe, K. *et al.* Characterization and mechanisms of action of novel NaV1.5 channel mutations associated with Brugada syndrome. *Circ Arrhythm Electrophysiol* **6**, 177-184 (2013). https://doi.org:10.1161/CIRCEP.112.974220
59 James, Z. M. & Zagotta, W. N. Structural insights into the mechanisms of CNBD channel function. *J Gen Physiol* **150**, 225-244 (2018). https://doi.org:10.1085/jgp.201711898
60 Whicher, J. R. & MacKinnon, R. Structure of the voltage-gated K^+ channel EAG1 reveals an alternative voltage sensing mechanism. *Science* **353**, 664-669 (2016). https://doi.org:10.1126/science.aaf8070
61 Moreau, A., Gosselin-Badaroudine, P. & Chahine, M. Molecular biology and biophysical properties of ion channel gating pores. *Q Rev Biophys* **47**, 364-388 (2014). https://doi.org:10.1017/S0033583514000109
62 Tombola, F., Pathak, M. M. & Isacoff, E. Y. Voltage-sensing arginines in a potassium channel permeate and occlude cation-selective pores. *Neuron* **45**, 379-388 (2005). https://doi.org:10.1016/j.neuron.2004.12.047
63 Tao, X., Lee, A., Limapichat, W., Dougherty, D. A. & MacKinnon, R. A gating charge transfer center in voltage sensors. *Science* **328**, 67-73 (2010). https://doi.org:10.1126/science.1185954
64 Vieira-Pires, R. S. & Morais-Cabral, J. H. 3_{10} helices in channels and other membrane proteins. *J Gen Physiol* **136**, 585-592 (2010). https://doi.org:10.1085/jgp.201010508
65 Burtscher, V. *et al.* Structural basis for hyperpolarization-dependent opening of human HCN1 channel. *Nat Commun* **15**, 5216 (2024). https://doi.org:10.1038/s41467-024-49599-x
66 Oliveira, B. L., Guo, Z. & Bernardes, G. J. L. Inverse electron demand Diels-Alder reactions in chemical biology. *Chem Soc Rev* **46**, 4895-4950 (2017). https://doi.org:10.1039/c7cs00184c
67 Jewett, J. C. & Bertozzi, C. R. Cu-free click cycloaddition reactions in chemical biology. *Chem Soc Rev* **39**, 1272-1279 (2010).
68 Dai, G. Neuronal KCNQ2/3 channels are recruited to lipid raft microdomains by palmitoylation of BACE1. *J Gen Physiol* **154** (2022). https://doi.org:10.1085/jgp.202112888
69 Dai, G., Yu, H., Kruse, M., Traynor-Kaplan, A. & Hille, B. Osmoregulatory inositol transporter SMIT1 modulates electrical activity by adjusting $PI(4,5)P_2$ levels. *Proc Natl Acad Sci U S A* **113**, E3290-3299 (2016). https://doi.org:10.1073/pnas.1606348113
70 Schmied, W. H., Elsasser, S. J., Uttamapinant, C. & Chin, J. W. Efficient multisite unnatural amino acid incorporation in mammalian cells via optimized pyrrolysyl tRNA synthetase/tRNA expression and engineered eRF1. *J Am Chem Soc* **136**, 15577-15583 (2014). https://doi.org:10.1021/ja5069728
71 Handlin, L. J. *et al.* Membrane Lipid Domains Modulate HCN Channels in Nociceptor DRG Neurons. *bioRxiv* (2024). https://doi.org:https://doi.org/10.1101/2023.09.02.556056
72 Gordon, S. E., Munari, M. & Zagotta, W. N. Visualizing conformational dynamics of proteins in solution and at the cell membrane. *Elife* **7** (2018). https://doi.org:10.7554/eLife.37248
73 Post, J. A., Verkleij, A. J. & Langer, G. A. Organization and function of sarcolemmal phospholipids in control and ischemic/reperfused cardiomyocytes. *J Mol Cell Cardiol* **27**, 749-760 (1995). https://doi.org:10.1016/0022-2828(95)90080-2
74 MacKerell, A. D. *et al.* All-atom empirical potential for molecular modeling and dynamics studies of proteins. *J Phys Chem B* **102**, 3586-3616 (1998). https://doi.org:10.1021/jp973084f
75 Phillips, J. C. *et al.* Scalable molecular dynamics with NAMD. *J Comput Chem* **26**, 1781-1802 (2005). https://doi.org:10.1002/jcc.20289
76 Phillips, J. C. *et al.* Scalable molecular dynamics on CPU and GPU architectures with NAMD. *J Chem Phys* **153**, 044130 (2020). https://doi.org:10.1063/5.0014475
77 Hoover, W. G. Canonical dynamics: Equilibrium phase-space distributions. *Phys Rev A Gen Phys* **31**, 1695-1697 (1985). https://doi.org:10.1103/physreva.31.1695

78 Feller, S. E., Zhang, Y. H., Pastor, R. W. & Brooks, B. R. Constant pressure molecular dynamics simulation: the Langevin piston method. *Journal of Chemical Physics* **103**, 4613-4621 (1995). https://doi.org:10.1063/1.470648

79 Martyna, G. J., Tobias, D. J. & Klein, M. L. Constant Pressure Molecular Dynamics Algorithms. *Journal of Chemical Physics* **101**, 4177-4189 (1994). https://doi.org:10.1063/1.467468

80 Pollock, E. L. & Glosli, J. Comments on P^3M, FMM, and the Ewald method for large periodic coulombic systems. *Computer Physics Communications* **95**, 93-110 (1996). https://doi.org:10.1016/0010-4655(96)00043-4

81 Wang, W. & MacKinnon, R. Cryo-EM Structure of the Open Human Ether-a-go-go-Related K^+ Channel hERG. *Cell* **169**, 422-430 e410 (2017). https://doi.org:10.1016/j.cell.2017.03.048